RESEARCH ARTICLE

Key Points:
- Wave climate of the Apostle Islands in Lake Superior for 35 year was hindcast
- Statistics of the wave climate reveal the spatial variability of wave properties
- An increasing trend of SWH is found due to climate change

Correspondence to:
C. H. Wu,
chinwu@engr.wisc.edu

Wave climatology in the Apostle Islands, Lake Superior

Joshua D. Anderson[1], Chin H. Wu[1], and David J. Schwab[2]

[1]Department of Civil and Environmental Engineering, University of Wisconsin-Madison, Madison, Wisconsin, USA, [2]U-M Water Center, University of Michigan, Ann Arbor, Michigan, USA

Abstract The wave climate of the Apostle Islands in Lake Superior for 35 year (1979–2013) was hindcast and examined using a third-generation spectral wave model. Wave measurements within the Apostle Islands and offshore NOAA buoys were used to validate the model. Statistics of the significant wave height, peak wave period, and mean wave direction were computed to reveal the spatial variability of wave properties within the archipelago for average and extreme events. Extreme value analysis was performed to estimate the significant wave height at the 1, 10, and 100 year return periods. Significant wave heights in the interior areas of the islands vary spatially but are approximately half those immediately offshore of the islands. Due to reduced winter ice cover and a clockwise shift in wind direction over the hindcast period, long-term trend analysis indicates an increasing trend of significant wave heights statistics by as much as 2% per year, which is approximately an order of magnitude greater than similar analysis performed in the global ocean for areas unaffected by ice. Two scientific questions related to wave climate are addressed. First, the wave climate change due to the relative role of changing wind fields or ice covers over the past 35 years was revealed. Second, potential bluff erosion affected by the change of wave climate and the trend of lower water levels in the Apostle Islands, Lake Superior was examined.

1. Introduction

Information about the wave climate is crucial to many environmental and societal issues. For example, in the Apostle Island, area of Lake Superior recreational boating involves tens of thousands of sailboats, motorboats, and kayaks per year [*Kraft et al.*, 2007]. Extreme wave conditions can pose navigation hazards for recreational watercraft and result in tragic drowning incidents (Duluth News Tribune, 12 September 2010 and 9 September 2011). Safe design of coastal and offshore structures also requires accurate knowledge of wave climate extremes [*Panchang et al.*, 2013]. Furthermore, wave climate can affect many geomorphic and ecologic processes. Particularly, coastal wave energy has been directly related to shoreline damage, property loss, and bluff recession [*Meadows et al.*, 1997; *Swenson et al.*, 2006; *Lin and Wu*, 2014]. Lakebed sediment resuspension has been shown to be dominated by wave-generated shear stress during large storm events [*Schwab et al.*, 2006]. Approximately 3% of the coastline in the Apostle Islands National Lakeshore of Lake Superior is designated as wetland [*Kraft et al.*, 2007], which is significantly affected by wave exposure [*Thomasen et al.*, 2013]. Last but not least, lake trout are economically important species that preferentially spawn in a threshold of elevated wave disturbance or turbulence [*Fitzsimons and Marsden*, 2014]. Spatial information about the wave climate can provide insight into the historical and present success of embryonic survival of lake trout in the Apostle Islands [*Coberly and Horrall*, 1980; *Schram et al.*, 1995]. In view of these important consequences, it is imperative to characterize wave climatology around the Apostle Islands in Lake Superior.

Determination of wave climate statistics often relies on analysis of historical wave records. Many of the aforementioned wave-dependent issues are assessed using the statistical distribution of three wave characteristics: Significant Wave Height (SWH), Mean Wave Direction (MWD), and Peak Wave Period (PWP), i.e., the period at the peak of the energy spectrum. To account for interannual variability, the World Meteorological Organization's (WMO) standard duration for an evaluation of climate is 30 years [*World Meteorological Organization*, 2007]. Historical measurements by the National Data Buoy Center of NOAA are the best candidate to meet this criterion. In the Great Lakes, these buoys have been in operation since the early 1980s, i.e., approximately 30 years. However, the spatial coverage of wave buoys is limited to a few locations per lake. The buoy locations are typically offshore, far away from coastal areas where wave characteristics are significantly altered by nearshore transformation processes. Consequently, wave hindcast through modeling is

usually employed to fill in the paucity of measured wave data and provide the spatial variability of wave climate [*Caires and Sterl*, 2005; *Jensen et al.*, 2012].

In the past, models for hindcasting wave data sets have been successfully applied to obtain wave climate statistics such as annual means, seasonal variability, return level estimates, correlation with atmospheric cycles, and long-term trends on both global [*Sterl and Caires*, 2005; *Chawla et al.*, 2013; *Stopa et al.*, 2013a] and regional scales [*Panchang et al.*, 2008; *Waters et al.*, 2009; *Dodet et al.*, 2010]. In the Great Lakes, hindcasting of the wave climate has been led by the U.S. Army Corps of Engineers under the Wave Information Studies (WIS) project [*Resio and Vincent*, 1978; *Hubertz et al.*, 1991; *Jensen et al.*, 2012]. Recently, the WIS project has completed a wave model hindcast for Lake Superior for the period from 1979 to 2012. Data from the WIS project include various products like historical time series of SWH, monthly means and maxima, extreme value analysis of SWH, and wave percent occurrence tables (http://wis.usace.army.mil/hindcasts. shtml). Nevertheless, data are limited to the selected WIS locations in the Lake Superior and do not include waves inside many sheltered areas, e.g., the Apostle Islands. While other operational wave models, including the Donelan model developed by the Great Lakes Environmental Research Laboratory in the early 1980s [*Liu et al.*, 1984] and Wave Watch III model developed by National Centers for Environmental Prediction with improved model physics [*Alves et al.*, 2014], have been used for Lake Superior, the overall grid resolutions range from 3 to 10 km. With the dimensions of the Apostle Islands as small as 250 m and adjacent islands separated by as little as 1 km, no wave hindcast data inside the islands have been reported.

Given the recent finding of climate change, assessing the future of the wave climate is increasingly important. In the ocean, wave climate trends have been quantified due to changes in wind speed and direction [*Caires and Sterl*, 2005; *Dodet et al.*, 2010]. In Lake Superior, increasing summer wind speeds over Lake Superior have been shown due to a decreased water-air temperature gradient [*Desai et al.*, 2009], supporting the finding that water temperatures are rising faster than the air [*Austin and Colman*, 2007]. *Liu and Ross* [1980] showed that unstable conditions can enhance wave growth when water temperatures are warmer than the air. Given the observed rise in water surface temperatures of Lake Superior and a lengthening of the stratified season [*Austin and Colman*, 2007], atmospheric unstability can further elevate the wave climate. Furthermore, trends of the wave climate in the Great Lakes can be affected by the observed loss of ice cover. *Schwab et al.* [2006] showed that decreased ice cover in the southern basin of Lake Michigan allowed for greater occurrence of large sediment resuspension events forced by waves. In the Apostle Islands, *Howk* [2009] showed that ice cover has been decreasing at a higher rate than the average rate of Lake Superior, suggesting that the wave climate in the Apostles is particularly susceptible to climate change. While much evidence exists to indicate the wave climate in the Apostle Islands is increasing, there has been no quantification of these trends in the Apostles or anywhere on the Great Lakes. Additionally, there has been little examination of how wave climate trends affected by ice loss compared to those found in areas unaffected by ice. Lastly, relative roles of winds and ice covers in modifying the wave climate in the Apostle Islands are unclear.

Bluff recession, strongly correlated with wave climate [S*wenson et al.*, 2006], is a significant issue affecting the economic development and property safely in the coastal community in the Great Lakes [*Angel*, 1995; *Meadows et al.*, 1997]. Conservation of the shoreline is crucially important in the Apostle Islands, possessing the largest collection of lighthouses in the National Park System [*Kraft et al.*, 2007]. In the past, characterization of coastal bluff stability and recession within the Apostles has had to be performed with the limited information of the wave climate [*Swenson et al.*, 2006; *Pendleton et al.*, 2007]. As a result, difficulties in projecting bluff recession in Lake Superior have been recognized and acknowledged. To remedy this issue, obtaining reliable wave climate are desperately needed since waves typically play a dominant role in the recession rates of coastal bluffs. For example, waves can elevate bluff recession by eroding nearby lakebed sediments, a process known as downcutting [*Lin and Wu*, 2014]. Additionally, waves can erode sediments at the toe of a bluff, resulting in a steeper slope that becomes unstable and is more prone to failure [*Brown et al.*, 2005]. Meanwhile, water levels can also affect bluff erosion by raising or lowering the impact height of waves on a bluff toe [*Meadows et al.*, 1997; *Castedo et al.*, 2013]. *Brown et al.* [2005] and *Swenson et al.* [2006] showed that bluff recession is correlated well with the magnitude-based wave impact height, defined as the elevation of wave runup minus the elevation of a bluff toe. While the mean water levels on Lake Superior have been steadily decreasing over the past 30 years [*Assel et al.*, 2004; *Gronewold et al.*, 2013], it is unclear if the lower lake levels reduce the elevated wave climate on overall impact of coastal bluffs in Apostle Islands.

The objective of this paper is to analyze the wave climate of the Apostle Islands in Lake Superior to the address the two science questions. First, how would the wave climate change due to changing wind fields or ice covers over the past 35 years? Second, how would the combined changing wave climate and the trend of lower water levels affect the coastal bluff erosion? To answer these questions, a wave model of Lake Superior with justifiable spatial resolution in the Apostle Islands region is developed and applied in a 35 year hindcast (1979–2013). Wave measurements collected within the Apostle Islands and from offshore NOAA buoys are used to validate the model. Statistics of the wave climate including significant wave height, peak wave period, and mean wave direction are obtained for average and extreme events. Extreme value analysis is performed to estimate the significant wave height for a range of return periods. Long-term trends of wave height are quantified to evaluate the effects of climate change on wave climate statistics. Finally, the effects of wave climate and low water level trend on bluff erosion are examined.

The paper is organized as follows. Description of the bathymetry and atmospheric climate in the Apostle Islands is provided in section 2. Section 3 describes the data sources for model inputs of wind and ice, wave model performance, the statistical methods applied in the analysis of the hindcast waves, and the method for bluff recession analysis. Section 4 presents the results of the hindcast including: statistics of three wave climate parameters (SWH, MWD, and PWP), return value estimates of SWH, long-term trends in SWH, and trends in wave impacts on coastal bluffs. Section 5 discusses the performance and limitation of wave modeling, effects of ice-time on wave statistics, the role of ice and wind on long-term wave climate statistics, and the role of water level and wave climate on bluff recession. Finally, a summary of the major findings from this study is given in section 6.

2. Study Site

The Apostle Islands are located off the Bayfield Peninsula (BP) in the western arm of Lake Superior. Including all 21 islands and the adjacent mainland, the site contains over 300 km of Great Lakes coastline [*Kraft et al.*, 2007]. Water depths within the archipelago are typically less than 60 m except for a deep channel in the east, which ranges from 100 to 140 m (see Figure 1). Along the northwestern boundary, waters are shallow with depths ranging from 40 m to less than 20 m. Multiple shoals and headlands exist predominantly at the outer edges of the island network with northeast alignment, most notably the Gull Shoal (GS) at the eastern exterior. A NOAA meterological station (DISW3), located on the northern boundary of the archipelago, has collected hourly wind measurements since 1983. The historical record of DISW3 indicates that the average wind speed is 5.03 m/s with a mean direction directly from the west. The strongest storm winds blow from the northeast but large westerly wind events are equally common. Ice cover has a high interannual variability and may be present from December to May [*Assel*, 2003; *Kraft et al.*, 2007]. Ice cover at the City of Bayfield, located on the eastern coast of the BP, has been decreasing at a rate of approximately 14.7 days per decade since 1975 [*Howk*, 2009].

3. Methods

3.1. Data

3.1.1. Wind Field

In this study, gridded 10 m winds (U_{10}) from the Climate Forecast System Reanalysis (CFSR) were used to drive the wave model. The CFSR products are produced by the National Center for Environmental Prediction (NCEP) using a coupled global atmospheric-oceanic-ice-land model with advanced data assimilation techniques and an extensive database of meteorological observations [*Saha et al.*, 2010]. The original CFSR data set spans from 1979 to 2010 and continues to operate as the second version of the Climate Forecast System (CFSv2) with multiple improvements over CFSR, including a higher spatial resolution [*Saha et al.*, 2014]. Spatial resolution of the CFSR is approximately 38 km (∼20 km for CFSv2) and temporal resolution is 1 h, a significant upgrade from previous global reanalysis products. The spatial resolution rivals focused regional products like the North American Regional Reanalysis. Data can be accessed through the National Center for Atmospheric Research (http://rda.ucar.edu/pub/cfsr.html).

Comparison of CFSR winds with measurements from meteorological stations at the study sites and offshore buoys was made here. Atmospheric stability, which can affect wave growth, was accounted for by adjusting CFSR gridded winds to an equivalent neutrally stable wind speed [*Liu and Schwab*, 1987]. Specifically, all
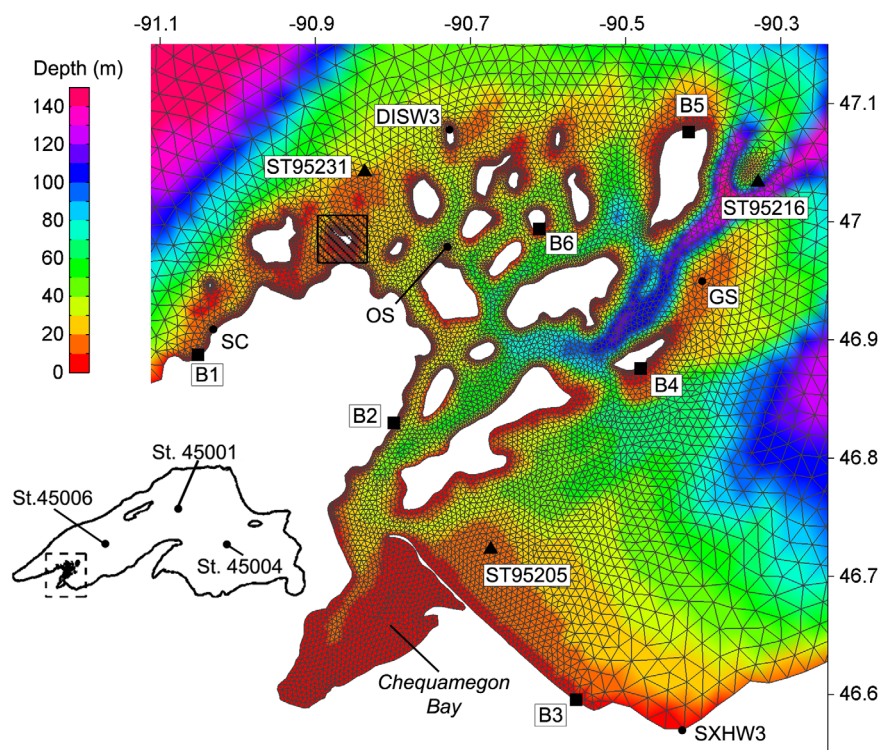
Figure 1. Apostle Islands bathymetry map and location on Lake Superior. Sites identified with a circle (•) are meteorological or wave observation stations. Sites identified with a triangle (▲) are USACE WIS stations. Sites identified with a square (■) are locations analyzed for wave impacts on bluffs. The unstructured SWAN mesh applied in the hindcast is overlaid on the map. The nonhydrostatic phase-resolving model domain is identified as a box filled with diagonal lines at approximately 47°N and −90.9°E.

measured data were converted to 10 m height using the Monin-Obukhov similarity theory. Figure 2 shows statistical comparisons of CFSR and measured winds at two coastal stations (DISW3 and SXHW3) and two off-shore buoy locations (St. 45006 and St. 45001). In general, CFSR winds match well with the observations, especially at large wind speeds, but CFSR winds slightly overpredict measured values (positive bias) with higher biases at the offshore buoys. Of the four stations shown, only SXHW3 was located in a land cell in the CFSR model. Consequently, CFSR underpredicts observed wind speeds presumably due to a higher drag coefficient implemented for land, which is consistent with findings of the CFSR winds near the land-sea interface in the ocean [*Chawla et al.*, 2013]. To account for this underprediction, we extrapolated CFSR wind magnitudes from sea/water grids to land grids and retained the original direction of the land grid. A better agreement between the extrapolated and measured winds at the higher quantiles is shown in Figure 2c (plus markers).

Water temperatures were obtained from the "Great Lakes Surface Environmental Analysis" product of the NOAA CoastWatch node at GLERL. Daily averaged lakewide surface temperatures from 1995 to 2013 were available and the long-term averaged temperatures (1992–2013) were used for years prior to 1995. Gridded air temperatures were from the CFSR data archive. An extrapolation technique similar to the technique used for gridded wind data was employed for air temperatures at the land-sea interface.

3.1.2. Ice Field

Ice that can impede wave formation and transmission was considered in the wave model hindcast. The interaction between waves and ice is a complex process that should be addressed in wave hindcast. In this study, we employed a common technique by masking model grids with land when ice concentration exceeded a particular threshold. Ice concentration is the area of ice cover divided by the total area of water. Previous studies have implemented a range of ice concentration thresholds ranging from 30 to 50% [*Hubertz et al.*, 1991; *Bennington et al.*, 2010; *Tuomi et al.*, 2011]. Furthermore we implemented a land mask by lowering water depths to zero when ice concentrations exceeded a threshold of 30% under the assumption that waves can be considered unaffected by ice for ice concentrations 30% and below [*Tuomi et al.*, 2011]. Great Lakes ice data prior to 2003 have been digitized to gridded fields, which are available at http://www.glerl.noaa.gov/
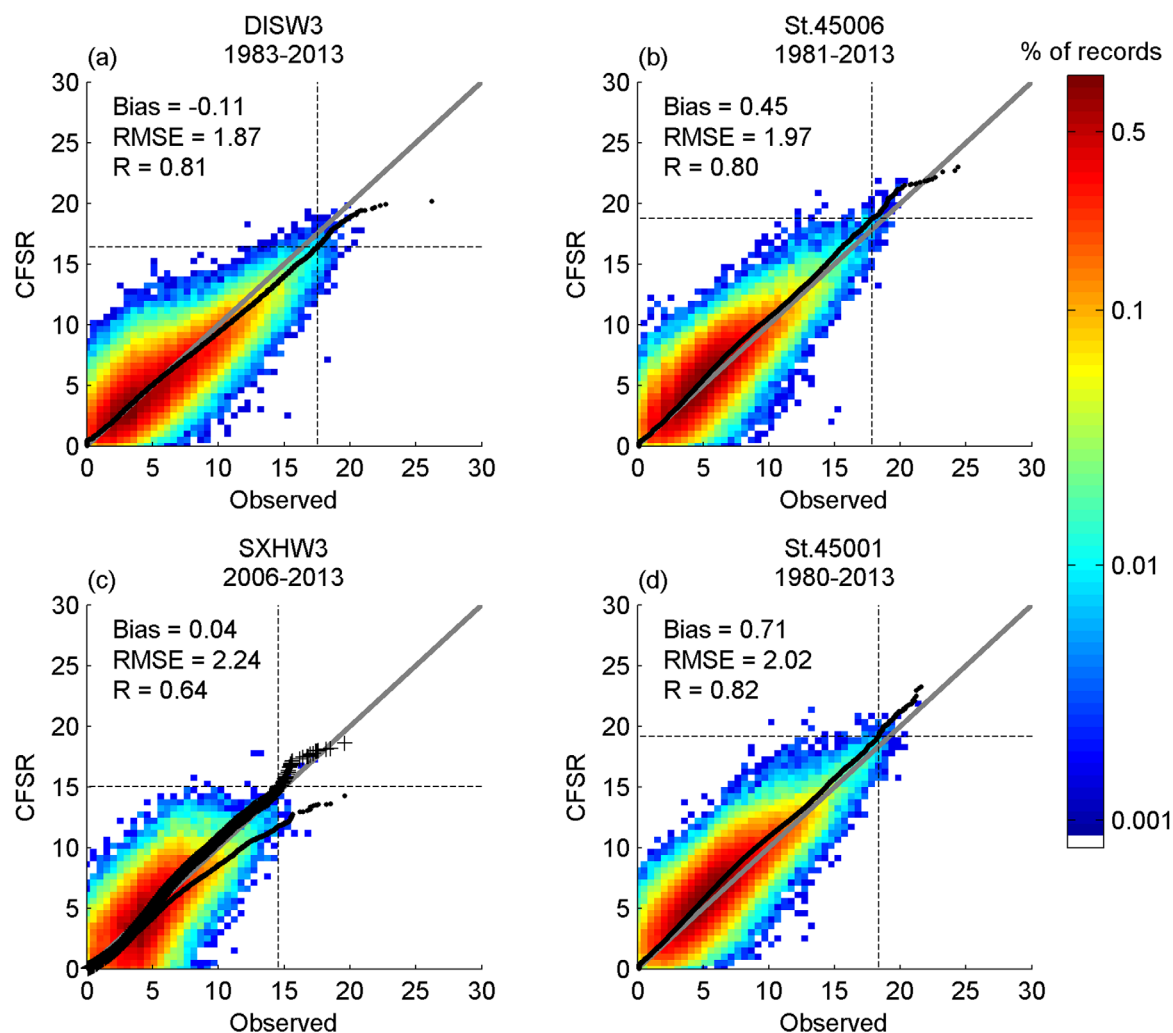
Figure 2. Scatter density plots of CFSR and observed U10 (m/s) at select locations. Color scaling is logarithmic and represents the percentage of hourly records occurring within a 0.5 × 0.5 m/s square. Also shown are Q-Q plots for raw CFSR and observed U10 (solid circle). At station (c) SXHW3, a Q-Q plot for the extrapolated oversea CFSR winds and observed winds is shown (plus). The vertical and horizontal dashed lines represent 99.9% quantile for each source. The thick grey line is the line of equivalence. Collection periods for the available observations are shown above each plot.

data/ice/atlas [*Assel*, 2003]. After 2003, gridded fields of ice concentration have been produced by the NOAA/ National Ice Center and can be obtained online (http://www.natice.noaa.gov/products/great_lakes.html). Gridded ice concentrations ranged from 0 to 99% and the spatial resolution ranged from 1.25 to 2.5 km. Ice concentration data were linearly interpolated in time to a daily resolution [*Assel*, 2005]. Spatial interpolation from gridded ice data to model grids was accomplished by the nearest neighbor technique.

3.1.3. Wave Measurements

Offshore wave data at the three buoys, Stations (St.) 45001, 45004, and 45006 (see Figure 1), were downloaded from the NOAA National Data Buoy Center. Dates of the measurements varied slightly for each buoy but nearly covered the full duration of the model hindcast (Table 1). Each buoy measured SWH and PWP during their collection periods, but only St. 45001 began measuring MWD in 2004. Further wave measurements within the Apostle Islands were collected at three sites (Figure 1) at various times between 2011 and 2013 (Table 1). At the GS and Oak Shoal (OS) sites, a 1 MHz Nortek Acoustic Wave and Current (AWAC), manufactured by Nortek AS, was deployed at approximately 12 m water depth. The AWAC uses a combination of acoustic surface track, pressure sensor, and acoustic velocimetry to measure SWH, PWP, and MWD [*Nortek AS*, 2005]. At the sea cave (SC) site, wave measurements were obtained using a single Acculevel pressure sensor, manufactured by Keller America, at 1.8 m above the bed in a water depth of 4 m. Pressure data were converted to bulk wave statistics with application of the linear transfer function and spectral analysis

Table 1. SWAN Model Hindcast Validation Statistics at Available Locations

Site	Record Duration	SWH				PWP				Direction	
		Bias (m)	RMSE (m)	SI	R	Bias (s)	RMSE (s)	SI	R	Bias (°)	RMSE (°)
SC	5 Jun 2011 to 11 Oct 2013	−0.02	0.12	0.47	0.85	−0.27	1.20	0.35	0.63		
OS	2 Jul 2013 to 1 Oct 2013	−0.03	0.10	0.44	0.77	−0.12	0.90	0.34	0.60	9.6	41.2
GS	11 Oct 2011 to 14 Jan 2012	0.06	0.18	0.26	0.92	0.04	1.00	0.25	0.76	3.2	34.8
St. 45006	22 Jun 1981 to 30 Nov 2013	−0.02	0.27	0.42	0.88	−0.25	0.99	0.25	0.76		
St. 45001	3 May 1979 to 31 Dec 2013	−0.02	0.30	0.37	0.90	−0.19	0.80	0.18	0.82	7.7[a]	32.0[a]
St. 45004	26 Apr 1980 to 23 Apr 2013	0.04	0.29	0.37	0.91	−0.08	0.79	0.18	0.81		
ST95231	1 Jan 1979 to 31 Dec 2012	0.04	0.15	0.38	0.94	0.22	0.83	0.25	0.85	2.5	35.7
ST95216	1 Jan 1979 to 31 Dec 2012	0.02	0.15	0.29	0.96	0.20	0.75	0.21	0.89	−1.5	28.7
ST95205	1 Jan 1979 to 31 Dec 2012	0.01	0.14	0.53	0.88	0.11	1.19	0.38	0.77	0.1	43.3

[a]Directional data limited to 21 April 2004 to 31 December 2013.

[*Sorensen*, 2006; *Jones and Monismith*, 2007], which has been shown to produce wave height estimates accurate to within 5% [*Bishop and Donelan*, 1987]. MWD estimates could not be determined from the pressure sensor, but MWD is most likely perpendicular to the shore due to refractive effects. Time series plots of the measured SWHs and PWPs during the most energetic conditions for each site will be shown and discussed in section 3.2.2.

3.2. Modeling

3.2.1. Wave Model

The third-generation spectral wave model, Simulating WAves Nearshore (SWAN), was used to estimate wave parameters in this study. A fully implicit numerical scheme was implemented to the SWAN model to remove the Courant stability criterion in explicit time stepping schemes [*Booij et al.*, 1999]. To further improve the efficiency, recent modifications include the development of a parallelized code structure and unstructured grids [*Zijlema*, 2010]. SWAN has been successfully applied to many coastal locations to examine wave climate [*Gorman et al.*, 2003; *Panchang et al.*, 2008; *Waters et al.*, 2009; *Stopa et al.*, 2013b].

In this study, we constructed an unstructured mesh for the whole of Lake Superior with higher resolution in the Apostle Islands. The mesh consisted of approximately 27,000 triangular elements ranging from a characteristic length of 5 km throughout the majority of the lake area to 100–500 m in the Apostle Islands region (Figure 1). Discretization in spectral space was set up with 50 logarithmically spaced frequency bands ranging from 0.05 to 5 Hz and 36 evenly spaced directional bands of 10°. The model time step was set to 10 min. All available source term formulations and tunable parameters were set to their default values [*SWAN Team*, 2013] except for wind growth and whitecap dissipation, which were set to the formulations commonly referred to as WAM cycle 4 [*Booij et al.*, 1999]. Currents and fluctuating water levels were omitted due to the uncertainty in the wind forcing, which is most commonly the dominant source of error in wave modeling [*Jensen et al.*, 2012]. To implement a land mask for ice cover, water surface elevations were set below bed elevations where ice was present. Model grids with zero water depth were effectively removed from the computational domain of the wave model and behaved similarly to land boundaries.

3.2.2. Calibration and Validation

The SWAN model was calibrated by varying two parameters in the whitecap dissipation formulation [*SWAN Team*, 2013]. The overall rate of whitecapping dissipation, C_{ds}, was varied with increments of 0.5 from 1.0 to 6.0, and the parameter which determines the dependency of whitecapping based on wave number, δ, was varied by increments of 0.2 from 0.0 to 1.0. Evaluation of the results was based on minimizing the root-mean-square error (RMSE) between the model and measured SWH at the SC and GS sites for the period 10–31 October 2011. The RMSE is defined by $RMSE = \sqrt{\frac{1}{N} \sum_{i=1}^{N} (M_i - O_i)^2}$, where N is the number of samples, M is model data, and O is observation data. Numerical tests revealed that both sites exhibited a similar response in RMSE to variations in the calibration parameters and that RMSE quantities were minimized when $C_{ds} = 3.5$ and $\delta = 1.0$. Default values for the SWAN model are $C_{ds} = 4.5$, $\delta = 0.5$; however, it is recommended to use $\delta = 1.0$ for better agreement of PWPs during low energy events while retuning C_{ds} [*SWAN Team*, 2013]. An application of SWAN in the Gulf of Mexico found $C_{ds} = 2.0$ and $\delta = 0.7$ provided the best fit [*Siadatmousavi et al.*, 2011].
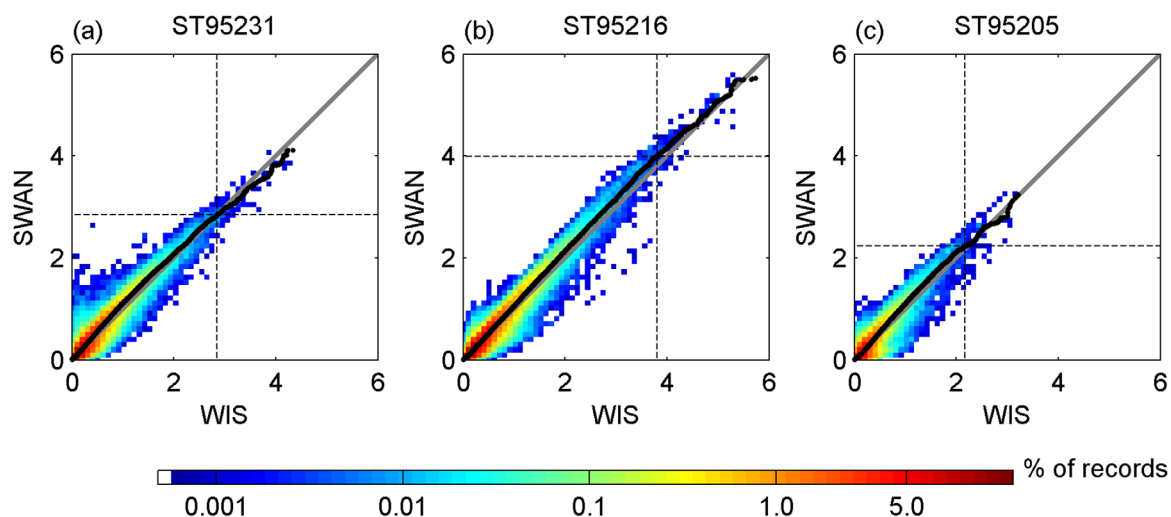
Figure 3. Scatter density plots of the SWAN and WIS modeled SWHs (m) at three locations (see Figure 1). Color scaling is logarithmic and represents the percentage of hourly records occurring within a 0.1 × 0.1 m². Also shown are Q-Q plots for SWAN and WIS SWHs (solid circle). The vertical and horizontal dashed lines represent the 99.9% quantile for each source. The thick grey line is the line of equivalence

Validation of model performance was based on statistical quantities commonly applied in wave modeling studies [*Gorman et al.*, 2003; *Stopa et al.*, 2013b]. Specifically, the bias $= \frac{1}{N} \sum_{i=1}^{N} (M_i - O_i)$, RMSE, scatter index (SI) $= \frac{RMSE}{\frac{1}{N} \sum_{i=1}^{N} O_i}$, and correlation coefficients (*R*) for SWH, PWP, and MWD were evaluated. For MWD, a limit of 180° was applied to error estimates (M-O) due to the circular nature of the property. Validation statistics were computed with two sources of data. First, we compared the SWAN model results to the USACE WIS hindcast results, which were computed with the WAM Cycle 4.5 wave model [*Jensen et al.*, 2012]. In this case, WIS model results replaced observed values (O) in the computation of the statistics. Table 1 shows the validation statistics at three WIS stations (ST95231, ST95216, and ST95205), located around the perimeter of the Apostle Islands (see Figure 1). In addition, we examined the scatter density and Q-Q plots of SWH to compare model results for extreme events (Figure 3). While differences exist between the two hindcast results, the two data sets correlate well. Second, we compared the SWAN model hindcast results to available in situ measurements. Table 1 summarizes the results for the three sites in the Apostle Island region and the three NOAA buoys. In general, the wave model performed reasonably well in predicting SWH with low biases and RMSEs. SI values for the SWHs are slightly higher than those reported in other studies [*Stopa et al.*, 2013; *Rusu and Guedes Soares*, 2012], but this may be explained by the comparatively small mean observed SWHs from this study, which is known to inflate SI values [*Ris et al.*, 1999]. Validation statistics for SWHs were comparable between measurement sites in the Apostle Islands and at open lake buoys with the exception of slightly better correlation coefficients at the buoys. Due to ambiguity in the spectral peak and wave direction during low energy conditions, estimates for PWP and MWD were limited to times when SWH > 0.15 m. Modeled PWPs were better at offshore locations with lower SI values by as much as a factor of 2. Validation statistics for the offshore buoys were also computed over the same time period as the nearshore Apostle Island data and a similar trend was found. The negative bias in PWP is due to a well-known limitation of SWAN during low energy conditions [*SWAN Team*, 2013]. An indication of better model performance during more energetic conditions is seen for the GS site, which was deployed during the fall and rarely experienced calm conditions. A statistical trend similar to PWP is seen for MWD. Overall, the model performance is consistent with the other modeling studies in that the validation statistics of wave modeling exhibits lower quality in sheltered and nearshore locations due to the more complex wave processes [*Rusu et al.*, 2008]. In addition, the accuracy at offshore locations increases since wave characteristics like PWP and MWD are better defined at larger values. For instance, when SWH > 0.5 m, wave direction RMSE values decrease to 16.8° and 23.2° for the OS and GS sites, respectively.

Figure 4 shows time series plots for SWH at the three measurement sites inside the Apostle Islands. Each time series spans 60 days of measurements and contains storms with dominant winds from the NE and NW (winds not shown here). Model wave heights match well with observations for both the peak and duration of storm events. Figure 5 shows time series plots of model and measured PWP for the same dates shown in
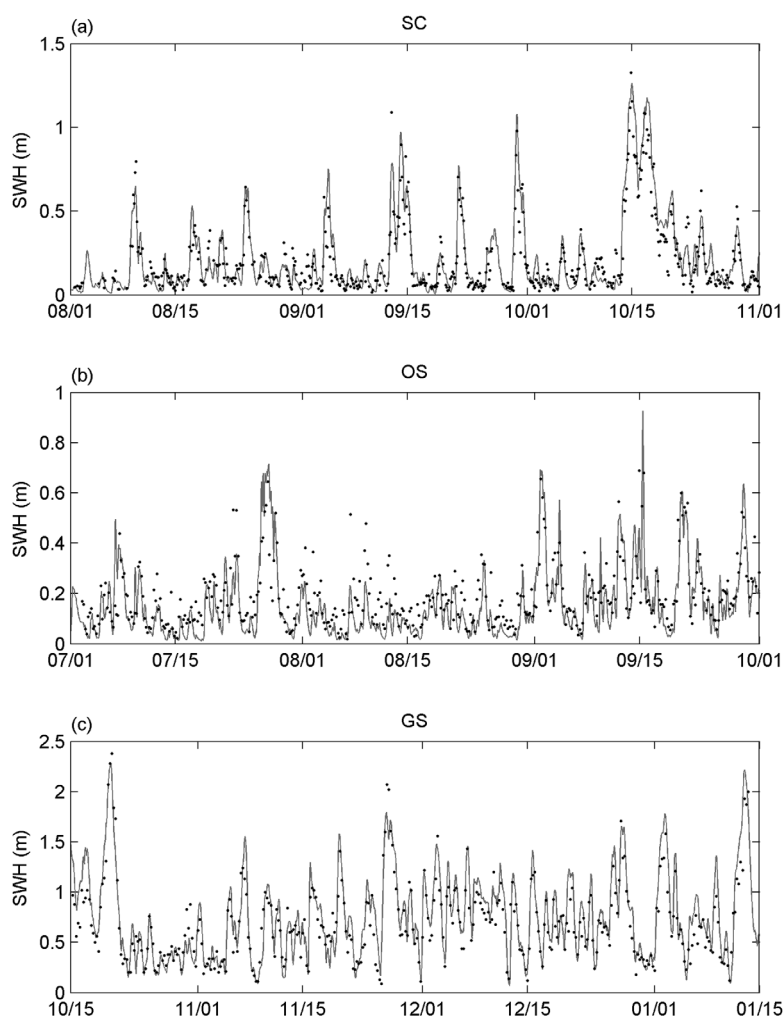
Figure 4. SWH comparisons of model (solid line) and measurements (solid circle) collected within the Apostle Islands. Due to the deployment schedule, collection years vary between sites: 2011 for SC, 2013 for OS, and 2011–2012 for GS.

Figure 4. Observed PWP measurements were excluded if SWH < 0.15 m. Overall, the SWAN model does a reasonable job capturing PWP magnitudes, especially during energetic conditions. However, a few instances of relatively large errors do exist (Figure 5a on 5 October, Figure 5c on 9 November), which may partially explain the larger error statistics at sites within the islands (Table 1). Short instances of swell are well predicted at the tail end of storm events, which can be seen most visibly in Figure 5a on 1 October. The model performs consistently in predicting storm events with various wind directions, demonstrating the reliability and accuracy of the model in simulating wind waves throughout the Apostle Islands.

3.3. Analysis
3.3.1. Wave Statistics
Statistics for the wave climate were based on the hourly model output over the duration of the hindcast with the omission of periods of ice. Effects of omitting ice covered periods in the calculation of wave climate statistics [*Tuomi et al.*, 2011] will be addressed in the discussion section. In this study, wave statistics including mean, 0.90 and 0.99 quantiles, and maximum values of SWH, PWP, and MWD were calculated. The decimal of the quantile specifies the fraction of the data that do not exceed the quantile value. Unlike calculating statistics of SWH from the entire hindcast record, statistics of PWP and MWD were based on conditions present during equivalent statistics of SWH. This definition was chosen because the maximum PWPs in the hindcast occurred as intermittent swell during small SWHs, e.g., see Figures 4 and 5 for the GS site on 31 December. So, the maximum PWP and MWD correspond to the values present during the maximum
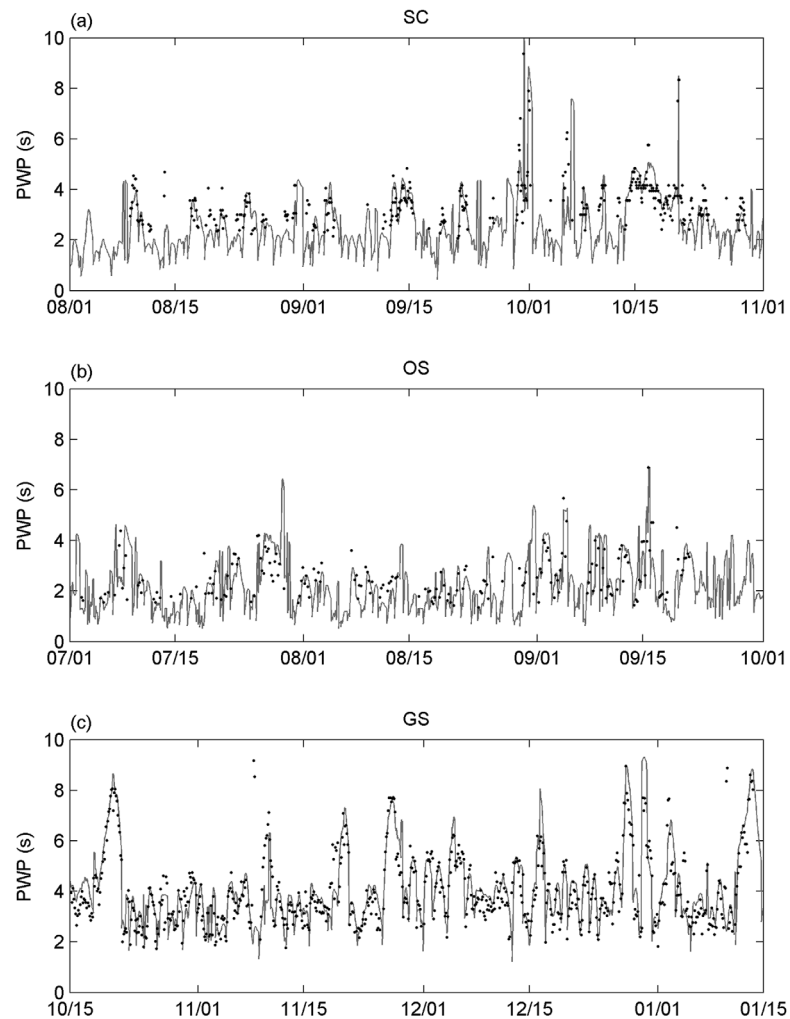
Figure 5. PWP comparisons of model (solid line) and measurements (solid circle) collected within the Apostle Islands. Estimates of PWP during low waves (H$_S$ < 0.15 m) were excluded from analysis. Years of the plots vary between sites and are the same as Figure 4.

SWH. Since a range of PWPs and MWDs occurred for a given quantile of SWH, a representative value was calculated by averaging PWPs or MWDs when the SWH was within ±1 cm of the quantile value. This method effectively determines the PWPs and MWDs that are most probable for a given quantile of SWH.

3.3.2. Extreme Value

Estimates of SWH at various return periods (i.e., 1, 10, and 100 years) were calculated at each element (location) in the model. The peaks-over-threshold (POT) method was applied to select independent events from the continuous time series of SWHs. Consecutive exceedances of the threshold (i.e., clusters) were considered as a single independent event from which only the maximum value was retained. Due to the variability of winds in a single storm, we required the temporal boundaries of consecutive clusters to be separated by at least 48 h [*Caires and Sterl*, 2005; *Aarnes et al.*, 2012] to further ensure only independent events were selected. Data sets selected by the POT method were assumed to be independently distributed with a generalized Pareto distribution (GPD) with a cumulative distribution function given by

$$F(x) = \begin{cases} 1 - \left(1 + \dfrac{\xi x}{\sigma}\right)^{-1/\xi} & \text{if } \xi \neq 0 \\ 1 - exp\left(\dfrac{-x}{\sigma}\right) & \text{if } \xi = 0, \end{cases} \qquad (1)$$

where *x* values are the POT selected data set minus the threshold and the range of *x* is $(0, \infty)$ if $\xi \leq 0$ and $(0, \sigma/\xi)$ if $\xi > 0$ [*Coles*, 2001]. The parameters ξ and σ are referred to as the shape and scale, respectively.

Shape and scale parameter estimates were fitted using the maximum likelihood approach. Evaluation of the fits was accomplished based upon the Anderson-Darling goodness-of-fit-test at the 5% significance level [*Choulakian and Stephens*, 2001]. The test allowed us to determine the validity of the fitted GPD and appropriate threshold values.

In this study, we used the 95% quantile of the complete SWH time series for the threshold, which yielded a valid fit of the GPD at 85% of model grids. For locations with invalid fits using the 95% quantile as the threshold, the quantile percentage was incrementally increased up to 99.5% until a valid fit was achieved. The quantile percentages applied in setting the thresholds here are within the range used in other studies: 93–97% [*Caires and Sterl*, 2005] and 99.7% [*Aarnes et al.*, 2012]. After determining the threshold value, we estimated the return value as

$$x_N = \begin{cases} \mu + \dfrac{\sigma}{\xi}\left[(\lambda N)^{\xi} - 1\right] & \text{if} \quad \xi \neq 0 \\ \mu + \sigma \log(\lambda N) & \text{if} \quad \xi = 0, \end{cases} \tag{2}$$

where μ is the threshold, λ is the average number of exceedance events per year, and N is the return period in years.

3.3.3. Long-Term Trends

To calculate long-term trends over the 35 year hindcast, the least squares linear regression fit was applied to annual statistics. Due to the winter ice season, we applied the common practice to calculate annual statistics based upon the climate year, defined as beginning and ending on June first [*Schwab et al.*, 2006]. The Mann-Kendall test [*McLeod et al.*, 1990; *Wang and Swail*, 2002] was used to assess the significance of a trend and trends were considered statistically significant with a p value less than 0.05, i.e., 95% confidence. Long-term trends of multiple variables were examined in this study: mean SWH, 0.90 and 0.99 quantiles of SWH, ice cover duration, mean wind speed, and mean wind direction.

3.3.4. Normalized Cumulative Wave Impact Height

Coastal bluff recession occurs when wave action erodes the bluff toe. A common index for bluff recession in the Great Lakes is the wave impact height (WIH), defined as the difference between wave runup and the bluff toe elevation:

$$WIH = MWL + R + S - TOE \tag{3}$$

where MWL is the mean water level elevation, R is the wave runup height, S is the wind setup, and TOE is the elevation of the bluff toe [*Brown et al.*, 2005]. *Swenson et al.* [2006] proposed cumulative wave impact height (CWIH), which is the positive WIHs integrated over a time period, to account for the frequency, duration, and magnitude of all wave events that act to erode a bluff toe.

In this study, we examine the trends in CWIH at six sites, as seen as solid squares in Figure 1. The three sites on the mainland (B1–B3) are colocated with ones analyzed in *Swenson et al.* [2006], and the three sites are located on the islands (B4–B6) identified as having high coastal change potential by *Pendleton et al.* [2007]. Sites B5 and B6 have historical lighthouses atop the bluff. To estimate the WIH at each location, equation (3) was applied. Mean water levels of Lake Superior were obtained at a monthly interval from the USACE-Detroit District over the hindcast period. Wave runup was calculated using the modified Mase method [*Melby*, 2012] with deep water wave heights and peak periods taken from model grids ~1 km offshore of a site. Beach slopes and toe elevations used in runup calculations were acquired from *Swenson et al.* [2006] for sites B1–B3 and estimated from photographs of the shores during visits to sites B4–B6. Wind setup and setdown were estimated with a linear force balance approach [*Sorensen*, 2006]. The WIH was estimated at each 1 h output from the hindcast. The $\overline{CWIH}$ was thereby calculated by integrating over each climate year and normalizing by the number of days in that year. A similar long-term trend analysis was performed on the $\overline{CWIH}$s over the hindcast period as described in section 3.3.3.

4. Results

In this section, the results from the 35 year hindcast are presented. Contour plots were generated to illustrate the spatial variability of the results within the Apostle Islands. To improve readability, contour plots were smoothed using a median filter over a 1 km^2 area.
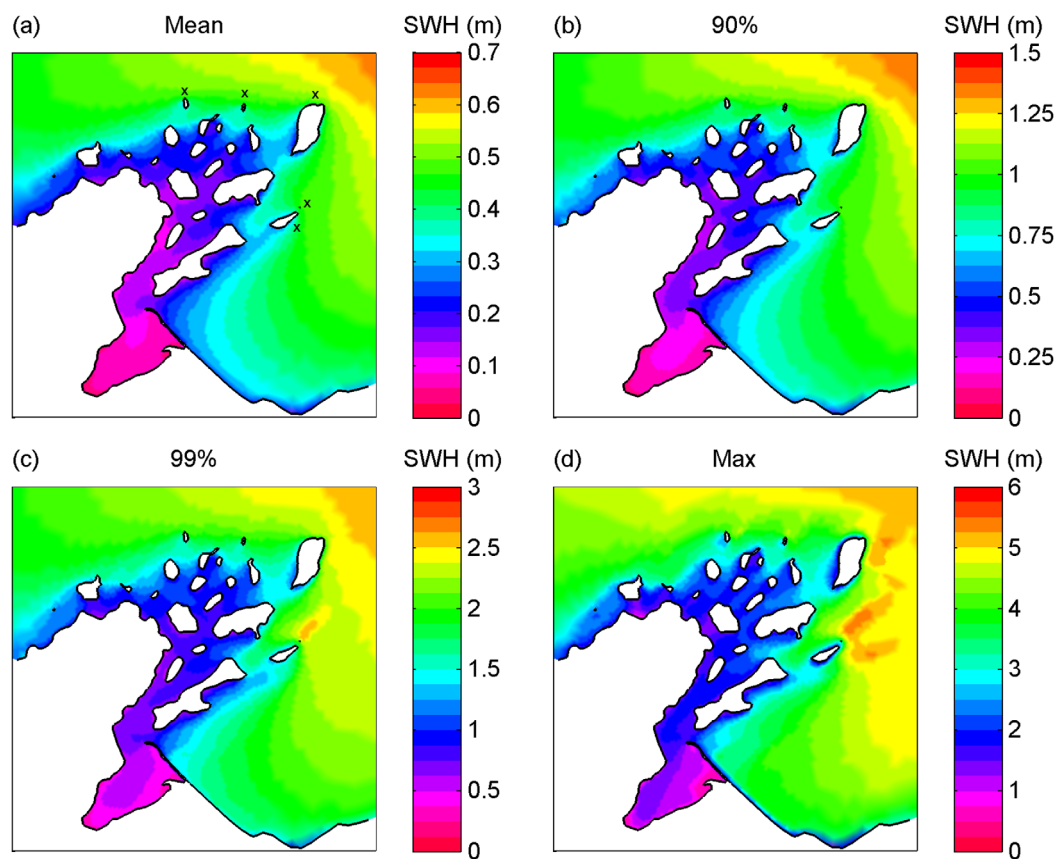
Figure 6. Statistics of SWH computed with hourly model output over the hindcast. (a) Mean, (b) 0.90 quantile, (c) 0.99 quantile, and (d) maximum. Exterior Islands are marked with cross in the plot of mean conditions (Figure 6a).

4.1. Wave Climate Statistics

Figure 6 shows SWH statistics with a consistent spatial pattern due to the attenuation of offshore waves caused by the effects of island sheltering. Two zones of SWHs are hereinafter referred to as the interior and exterior. The exterior zone includes nearby open waters and five islands (cross in Figure 6a) that lie along the northern and eastern extent of the archipelago. Two of these exterior islands are located immediately south-west of the GS, but one is barely visible at the scale of Figure 6. The interior includes the remainder of the Apostle Islands except for Chequamegon Bay (see Figure 1). Exterior SWHs are approximately 0.5, 1, 2, and 4 m for the mean, 0.90 quantile, 0.99 quantile, and maximum, respectively. Generally, interior SWHs are approximately half those experienced in the exterior for each statistic. Two deviations from this generality of SWH statistics are noticed here. First, refraction processes focus wave energy to increase SWHs at shoals and headlands within the exterior. This process is seen in the 0.99 quantile of SWH at the GS (Figure 6c) and becomes more widespread in the maximum SWHs (see Figure 6d), including the two small northernmost islands. The largest SWHs occur at the GS with a maximum SWH of 5.52 m during the hindcast. Second, a devi-ation is seen at the most sheltered locations of the interior, i.e., the eastern side of the BP. In this area, SWHs are smaller than the rest of the interior in the mean (Figure 6a). During larger events (Figure 6d), SWHs within the interior become more uniform as offshore wave energy penetrates deeper into islands. Signs also exist of the boundary between the exterior and interior moving further into the archipelago. Furthermore, Chequame-gon Bay is also affected by the increased penetration of wave energy during extreme conditions with mean SWHs less than 0.1 m and maximum SWHs as large as 1.5 m. In short, the spatial pattern of SWHs is generally consistent for all statistics due to the sheltering effect of the islands. The discrepancies are caused by wave refraction in the exterior and penetration of offshore wave energy into the sheltered areas of the interior.

PWP statistics can help to characterize the sea state by indicating the steepness of waves and the origin of their formation. Furthermore, PWP is important for many wave-dependent processes like lakebed sediment resuspension [*Schwab et al.*, 2006] and bluff erosion [*Brown et al.*, 2005; *Swenson et al.*, 2006]. Since waves that

Table 2. Percent Occurrence of SWHs and PWPs at the OS Site

SWH (m)	PWP (s)									Total
	<2	2–3	3–4	4–5	5–6	6–7	7–8	8–9	9–10	
0.00–0.25	29.759	18.361	12.517	5.509	1.561	0.871	0.342	0.130	0.038	69.088
0.25–0.50	0.300	8.514	6.325	2.732	0.677	0.464	0.214	0.058	0.011	19.295
0.50–0.75			1.087	4.095	1.747	0.318	0.101	0.088	0.056	0.014	7.506
0.75–1.00			0.010	1.120	1.328	0.211	0.040	0.015	0.017	0.016	2.757
1.00–1.25			0.001	0.230	0.498	0.197	0.009		0.002	0.005	0.942
1.25–1.50				0.009	0.189	0.131	0.004				0.333
1.50–1.75					0.042	0.026	0.003				0.071
1.75–2.00					0.006	0.002					0.008
Total	30.059	27.973	24.296	12.051	3.123	1.492	0.659	0.263	0.084	100.000

approach the Apostle Islands are generated over a range of fetch distances, different PWPs can occur for a specific SWH. In other words, PWP and SWH are not perfectly correlated. Table 2 shows the percent occurrence for PWP and SWH at the OS site over the model hindcast period. PWPs are seen to occur over a wide range when SWHs are small. The range narrows for the largest SWHs, indicating the dominance of wind waves over swell (large wave period like 9–10 s) for the largest events. Using the methods outlined in section 3.3, the PWPs corresponding to the SWH statistics for the OS site are 2.9, 3.7, 4.5, and 5.2 s for the mean, 0.90 quantile, 0.99 quantile, and maximum, respectively. Statistics computed directly from the record of PWPs would be 2.9, 4.5, 7.0, and 9.9 s for the mean, 0.90 quantile, 0.99 quantile, and maximum, respectively. The difference between these two methods of estimating PWPs is substantial for the most energetic events. In short the above comparison justifies the method here to estimate PWP that is most probable for a given SWH.

Figure 7 displays the computed PWPs that correspond to the SWH statistics. Like the SWHs, PWP exhibits a similar spatial pattern with clear distinction between the exterior and interior due to island sheltering. Mean
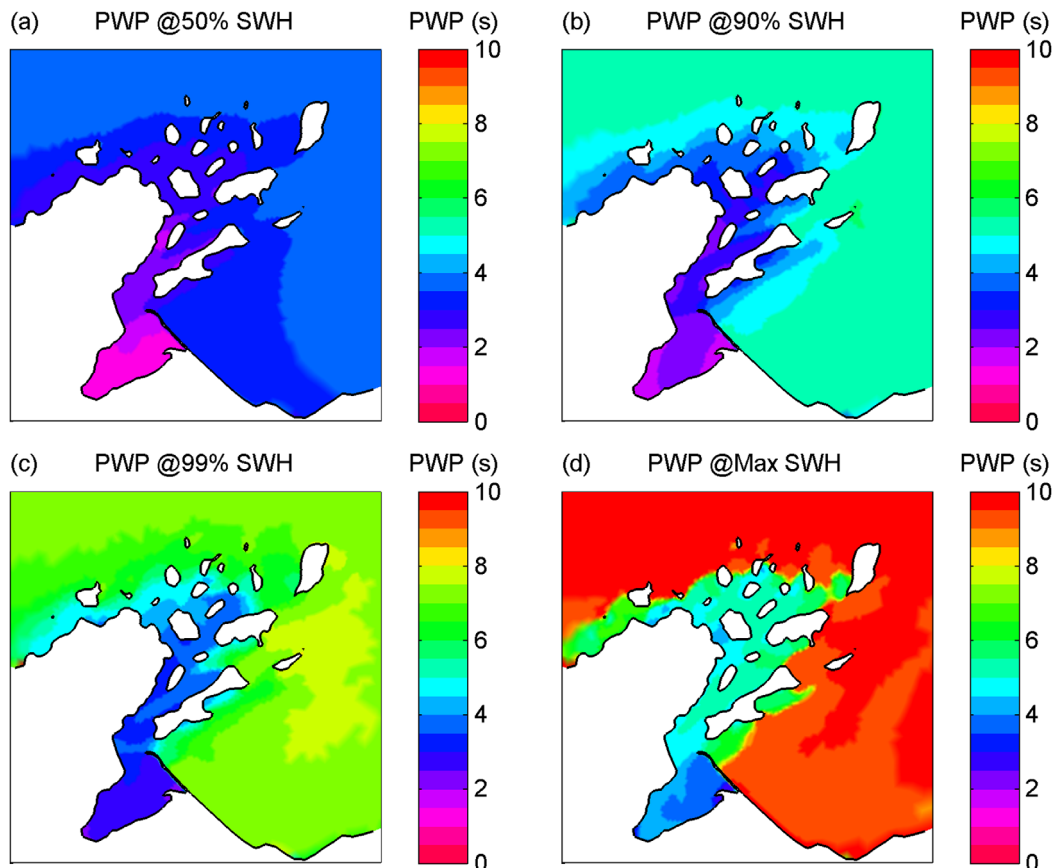

Figure 7. PWP statistics corresponding to the SWHs shown in Figure 6.
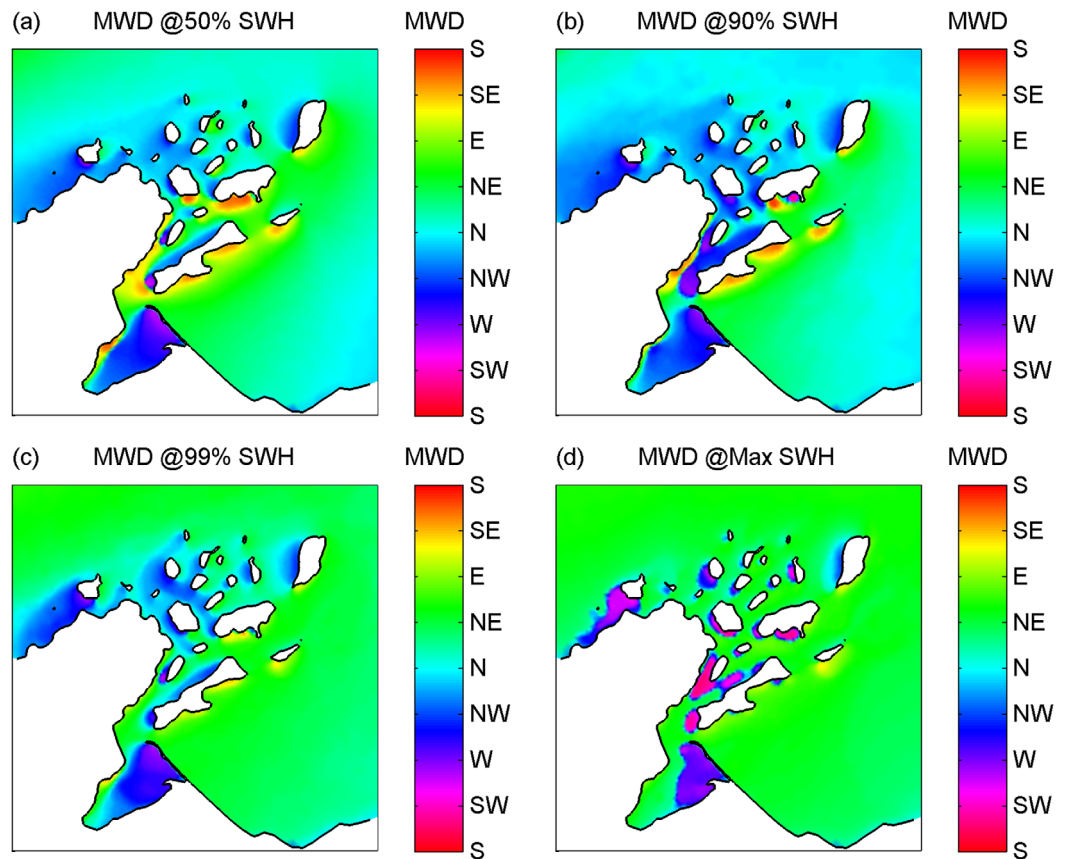
Figure 8. MWD statistics corresponding to the SWHs shown in Figure 6.

PWPs are below 4 s for most of the exterior and range from 2 to 3 s in the interior, with the smallest values occurring at the eastern side of the BP. For larger waves, PWPs for the exterior (interior) are approximately 5.5 (2.5–4), 7(3.5–4.5), and 10(5.0–6.0) s at the 0.90 quantile, 0.99 quantile, and maximum of SWH, respectively. For the maximum SWHs, a large attenuation gradient exists between the exterior and interior PWPs. Note that the method of determining maximum PWPs in Figure 7d can be generated from multiple separate events. Nevertheless results after performing analysis of a single extreme event (not shown here) exhibit a strong gradient of PWPs existed with similar magnitudes, suggesting that transmission of offshore wave energy into the interior is dominated by wave spreading, rather than direct wave propagation. Previous studies show that smaller period components in a two-dimensional wave spectrum spread more than higher period components [*Sorensen*, 2006; *Ardhuin and Roland*, 2012]. Therefore, the boundary of the interior and exterior seems to be where waves can no longer propagate directly from offshore due to island blocking and where the transmission of offshore wave energy is limited to spreading. Furthermore, the deviation in interior PWPs could be also caused by locally generated waves.

Figure 8 displays the MWDs corresponding to the SWH statistics. Offshore mean MWDs approach the islands approximately from the north due to east and west components that balance out on the average. Within the Apostle Islands, mean MWDs (see Figure 8a) are more westerly in the west and more easterly in the east, which is caused by the spreading of offshore waves around the islands. Interestingly, the MWDs for the 0.90 quantile of SWH (see Figure 8b) are slightly more westerly than the mean, suggesting that moderate events are typically generated by westerly winds. The MWDs for the 0.99 quantile of SWH (see Figure 8c) are dominated by waves traveling from the northeast in the offshore, northern and eastern regions. Nevertheless in the west and much of the central region of the islands, MWDs remain from the northwest. The MWDs corresponding to the maximum SWHs (see Figure 8d) are predominantly from the northeast and forced by strong northeast winds. Sheltered locations on the southwest side of islands, however, have westerly MWDs and are generated from westerly winds, rather than northeast wind generated waves that
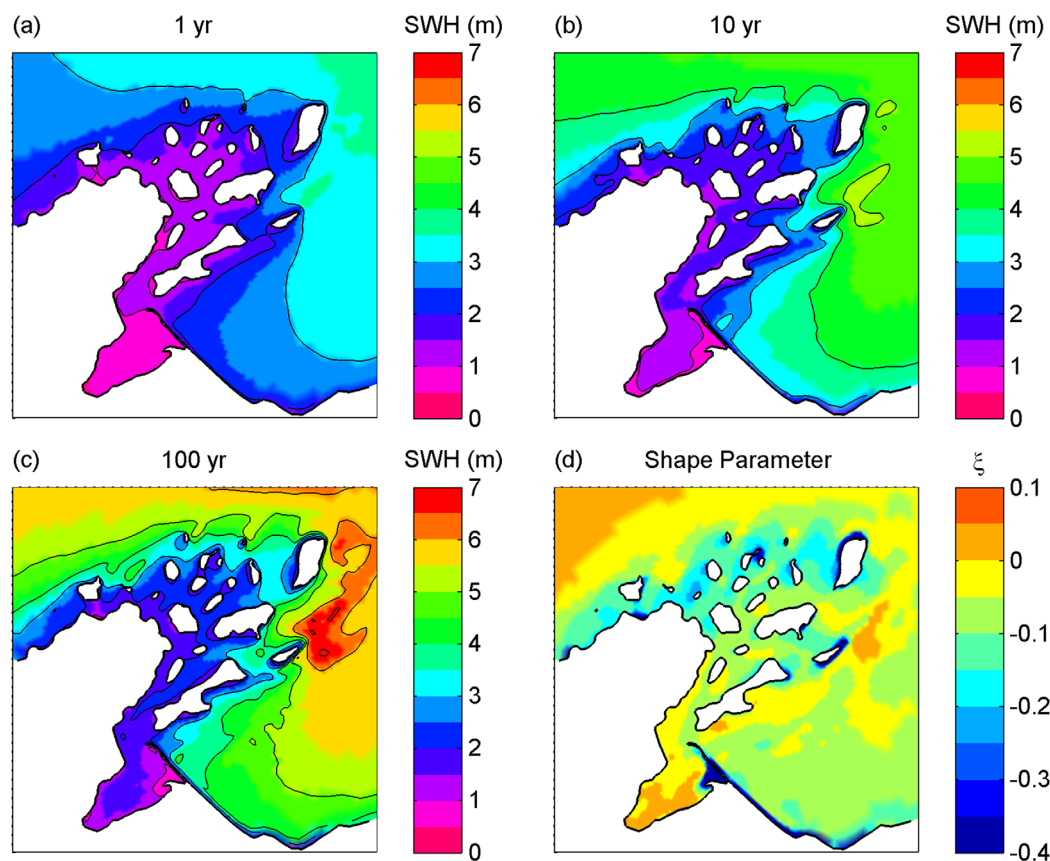
Figure 9. Return values of SWH at the (a) 1 year, (b) 10 year, and (c) 100 year return period with contours (black lines) spaced at 1 m intervals. (d) Shape parameter values from the fitted GPD.

have refracted or spread around an island. In general, the largest waves in the Apostle Islands have a northeast MWD and are oriented with the largest fetch over Lake Superior. Island sheltering causes many areas and shorelines to be more susceptible to westerly MWDs.

4.2. Extreme Values

Figure 9 shows the estimated values of SWH at the 1, 10, and 100 year return periods. The spatial patterns are similar to those observed in the mean and quantile plots of SWH with interior values being approximately half of those at the exterior. The 1 year return values of SWH are approximately 2.5–3 m around the exterior of the islands and range between 1 and 2 m within the interior. The 10 year return values are similar to the maximum values from the hindcast (Figure 6d) with SWHs approximately 3–4 m at the exterior and 1.5–2.5 m within the interior. The 100 year return values of SWH range from approximately 4–5 m around much of the exterior, 2–2.5 m for much of the interior and 1.5–2 m along the BP. The GS has the largest return values of SWH at 6.9 m. In comparison with the estimate based upon the JONSWAP fetch limited relation [*Hasselmann et al.*, 1976] using the maximum wind speed of 20 m/s (Figure 2) and the fetch of 340 km to the northeast of the Apostle Islands, the predicted SWH is 6 m. Note that the wind records from 1979 to 2013 never exceeded the 16 h duration for fetch limited waves at 20 m/s. Therefore, the actual wave height is likely less than 6 m. The elevated values at GS, other shoals, and headlands around the exterior are likely attributed to refractive focusing, which are also suggested in other studies [*Rusu and Guedes Soares*, 2012; *Tuomi et al.*, 2014]. Overall, it is suggested that refractive focusing causes the 100 year return value estimates of SWH at the GS to be among the greatest in all of western Lake Superior, even offshore waters. Finally, the shape parameters from the fitted GPDs are mostly negative in the study area (Figure 9d), suggesting that a Pareto distribution is more appropriate in the Apostle Islands than an exponential distribution (shape parameter of zero) universally applicable in the oceans [*Caires and Sterl*, 2005].
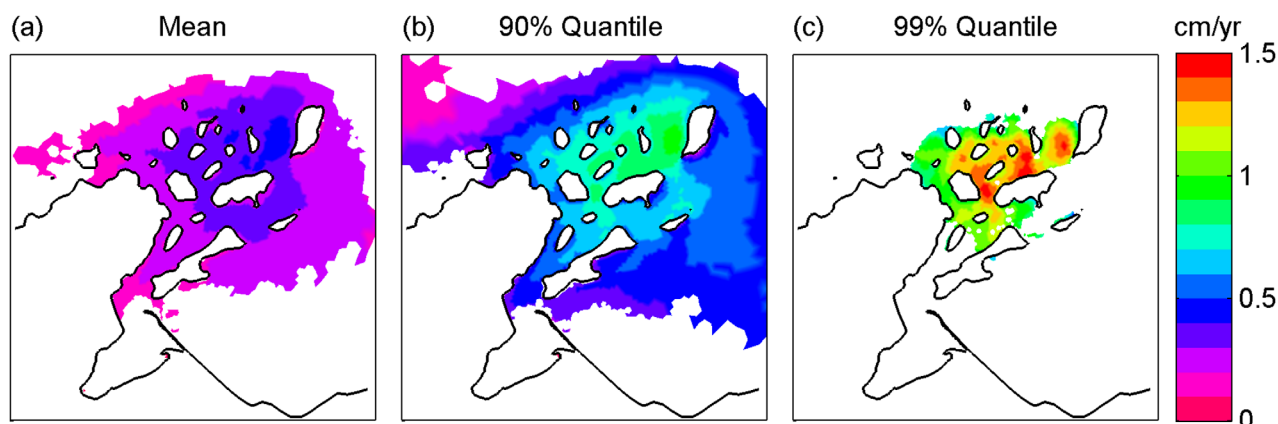
Figure 10. Contour plots of long-term trends of SWH for the (a) mean, (b) 0.90 and (c) 0.99 quantile. Only locations where trends are significant at 95% confidence are shaded.

4.3. Long-Term Trends

Figure 10 shows the long-term SWH trends for the mean, 0.90 and 0.99 quantiles at locations in which linear trends are significant at 95% confidence. All trends reported below are within the margin of modeling errors. The spatial coverage of significant trends is the largest for the 0.90 quantile and the smallest for the 0.99 quantile. Few locations in nearby offshore waters have significant trends. In general, there is an increasing trend in SWH, characterized by the slope value in cm/yr, over the 35 year hindcast duration. The maximum slopes occur in the northeast region of the Apostle Islands for each statistic and decrease radially outward. Spatial patterns of the slope between the mean and larger quantiles are similar but the magnitudes increase with larger quantiles. Peak trend magnitudes for the mean, 0.90 quantile, and 0.99 quantile are 0.45, 0.95, and 1.45 cm/yr, respectively. The trends in SWH expressed as a percentage of their respective values (see Figure 6) range between 0.5% and 2.0% per year, which are approximately an order of magnitude greater than those seen in other studies [*Caires and Sterl*, 2005; *Dodet et al.*, 2010]. The difference between our results and those in the ocean is attributed to existence of ice. The trend of reduced ice cover at our study site exposes waters to winter winds, which are greater than the rest of the year and produce larger waves. This explains the relatively higher percentage increase in SWHs observed in this study compared to other studies where ice was not a factor. Finally, the ratio between maximum slopes at the 0.99 quantile and the mean is approximately three. Interestingly, similar relationships between mean and larger quantiles of SWH were observed in the global ocean [*Caires and Sterl*, 2005], but the ratio between maximum slopes at the 0.99 quantile and the mean were approximately two.

4.4. Long-Term Trends in $\overline{CWIH}$

The trends in $\overline{CWIH}$s analyzed at the six sites, B1–B6, using the hindcast results are shown in Figure 11. Due to a combination of offshore SWH magnitudes, beach slope, and toe elevations (Table 3), the $\overline{CWIH}$ magnitudes increase from sites B1 to B6. Site B6 has the largest $\overline{CWIH}$s because the toe of the bluff meets the water level. A linear trend is used to fit the time series of annual $\overline{CWIH}$s for each site (see the bold solid lines). In general, a decreasing trend in $\overline{CWIH}$ is observed over the hindcast except that site B1 has the smallest $\overline{CWIH}$s and multiple years with zero $\overline{CWIH}$ due to a mild beach slope and the largest toe elevation. While only site B4 has the significant trend with a p value less than 0.05, the trends at the rest of the sites may still provide general patterns of $\overline{CWIH}$s. Site B6 is located in an area with among the significant trends of increasing SWHs (see Figure 10) and has the least significant trend in $\overline{CWIH}$ ($p = 0.79$) or essentially no change in $\overline{CWIH}$. Negative trends in $\overline{CWIH}$s are observed because of the statistically significant decreasing water level trend of -1.2 cm/yr in Lake Superior over the hindcast period [*Assel et al.*, 2004; *Gronewold et al.*, 2013]. Overall, the results suggest that decreasing water levels reduce coastal bluff erosion in most of the Apostle Islands but at areas where the SWHs are increasing the most can offset the reduction and elevate bluff recession rates. Further analysis of the effects of water level on these results is examined in the discussion section.
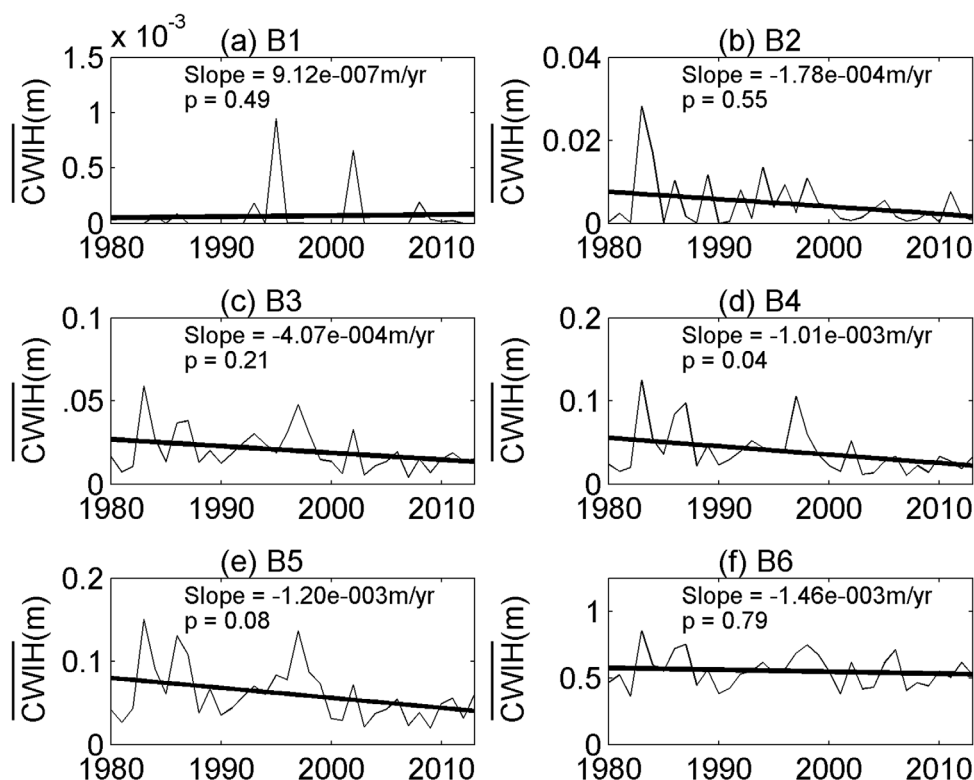
Figure 11. Time series of $\overline{CWIH}$ at each of the six sites B1–B6 (thin line) and linear trends (bold lines). Also shown are the trends and p values.

5. Discussion

5.1. Performance and Limitation of Wave Modeling

The SWAN wave model has been successfully applied to examine coastal wave climates [*Panchang et al.*, 2008; *Stopa et al.*, 2013b]. In this study, the resulting wave climate shows that offshore wave energy is attenuated at the exterior of the Apostle Islands with significantly smaller SWHs and PWPs in the interior. Many applications of third-generation spectral models, including SWAN, show similar sheltering effects from islands [*Ponce de Leon and Guedes Soares*, 2010; *Stopa et al.*, 2013b; *Tuomi et al.*, 2014]. Our validation statistics (see Table 1) demonstrates the capability of SWAN to reasonably simulate properties of the wave field within and around the islands. Specifically refraction, a wave process known to concentrate wave energy at bathymetrical features like shoals and headlands, seems to be well modeled by SWAN [*Rusu and Guedes Soares*, 2012; *Tuomi et al.*, 2014]. Wave measurements at the GS site have among the best validation statistics of all sites examined. The largest events in Figures 4c and 5c exhibit refractive focusing that is well captured by the model. On the other hand, Table 1 also shows that the SI and R statistics are slightly better at offshore buoys compared to the OS and SC sites. A similar degradation of model validation statistics near islands has been reported, suggesting that inaccuracies in modeling complex nearshore wave processes may be the cause [*Rusu et al.*, 2008]. Therefore, it is of importance to consider the limitations of our application of SWAN in simulating the wave sheltering effects from islands.

Table 3. Beach Slopes and Toe Elevations of Bluff Erosion Sites[a]

Site	Slope (°)	Toe Elevation (m)
B1	5.0	1.8
B2	14.0	0.8
B3	6.5	1.2
B4	5.0	0.8
B5	7.4	1.1
B6	30.0	0.0

[a]Toe elevations are referenced to the IGLD 1985 (~183.3 m).

Wave reflection was omitted in our application of SWAN due to insufficient information in the Apostle Islands. In other words, all wave energy that approached a coastline is dissipated completely in the model. While this is a reasonable approximation for most of the gently sloping coastlines [*Elgar et al.*, 1994], it may overestimate dissipation at 25% of the coastlines that are composed of exposed rocky cliffs [*Kraft et al.*, 2007]. The SC site is located near such a coast

and reflection may have caused the negative bias and slightly poorer SI and R for SWHs (Table 1). However, the differences in the validation statistics at the SC site compared to the other sites are relatively minor. Comparison of the time series shown in Figure 4a does not show a large bias during large events, suggesting that the reflection effects are relatively small. To further examine the potential spatial extent of reflection on the model results, a test case for reflection is setup in SWAN for a 2500 m × 2500 m domain containing one island (see a box filled with diagonal lines in Figure 1). To the northern boundary of the domain, we apply a constant 2-D wave spectrum, obtained from the hindcast results during an extreme northerly wind event. Both simulations with a reflection coefficient of 0.4 and without reflection are run and compared. The differences at the coast range from 7 to 10% of the incident SWH and reduce to less than 5% at approximately 300 m or 7 wavelengths of the PWP. Overall, these differences are relatively localized near the coast and are unlikely to significantly impact the results elsewhere. While reflection coefficients up to 0.4 have been reported for ocean swell reflecting off shorelines with steep cliffs [*O'Reilly et al.*, 1999], the reflection coefficients in the Apostles are likely smaller due to smaller wave periods typically occurring in the study area [*Elgar et al.*, 1994; *Ardhuin and Roland*, 2012]. The relatively good agreement with measurements at the SC site suggests that wave reflection has a minor impact on the wave climate in Apostle Islands.

Wave diffraction was omitted in the hindcast modeling results. An approximated formulation for diffraction in phase-averaged spectral models, like SWAN, has been proven effective but requires fine grid resolutions, which are computationally expensive [*Holthuijsen et al.*, 2003]. This formulation has been shown to influence large regions of the wave field on the lee side of islands in the ocean with the structured grid version of SWAN [*Rusu et al.*, 2008]. We test the effects of diffraction in our SWAN model for a 20 day period including a storm equivalent to a 10 year event (Figure 9b). Model runs are configured with and without the formulation for diffraction. Statistics of the SWH and PWP are compared. The maximum percent difference in the mean, 0.90 quantile, 0.99 quantile, and maximum values at any location are 0.1, 0.5, 0.3, and 0.3%, respectively. One reason for the minor effects of diffraction in this region is short-crested wind wave climate, which typically exhibit higher spreading rates than long-crested swell and diminish diffraction effects [*Holthuijsen et al.*, 2003; *Lin*, 2013]. Another possible reason for minor diffraction effects may be the use of the first-order upwind scheme employed in the unstructured SWAN model [*Zijlema*, 2010], which mimics some of the effects of diffraction through numerical diffusion.

To further examine the process of diffraction and numerical diffusion, we employ a phase-resolving nonhydrostatic model capable of modeling refraction and diffraction of surface waves propagating from deep to shallow water [*Young et al.*, 2009; *Wu et al.*, 2010]. The same domain (see a box filled with diagonal lines in Figure 1) is discretized using a 3000 m × 3000 m horizontal grid resolution. Reflections at the boundary are damped using a sponge layer in the nonhydrostatic model [*Yuan and Wu*, 2006]. The 2-D forcing spectrum conditions described previously in the reflection test are used. To eliminate refraction effects and examine diffraction alone, depths are set at a constant 20 m deep water condition. Five vertical layers are used in the nonhydrostatic model. A replicate run of the nonhydrostatic model is also completed in a SWAN model. The differences between the SWAN hindcast implementation and nonhydrostatic model results ranges between 5 and 8% of the incident SWHs in the shadow of the island and are approximately −3% just outside the shadow zone. Further refining the grid resolution in SWAN show little difference in these results, illustrating that errors from neglecting diffraction are likely less than those caused by numerical diffusion in our hindcast results. Numerical diffusion in the unstructured version of SWAN causes SWHs to be slightly over predicts in the shadow zone on the lee side of islands and slightly under predicts just outside the shadow zone. The errors caused by the numerical diffusion are deemed to be relatively minor and are likely even less considering wind forcing was removed from these comparisons.

Gridded wind fields are likely the main limitation of the results, given the relatively minor effects of omitted wave processes. Although the CFSR winds compared well with available observations (Figure 2), the reanalysis model did not resolve the effects of the islands on the wind field. This may partially explain the better performance of the model at open lake buoys. *Tuomi et al.* [2014] discussed that a reduction in winds in archipelagos may occur due to the drag of the islands. Since we extrapolated CFSR oversea winds at coastal locations, winds may have been slightly overestimated within the interior. However, the most sheltered observation locations (SC and OS) showed a negative bias (Table 1). It is likely that winds are increased through a funneling effect that has been observed in other island networks [*Stopa et al.*, 2013b]. To test the effects of wind errors on the results, sensitivity analysis was performed by scaling winds within the exterior and interior by −20%, −10%, 10%, and 20% over the climate year, June 2007 to June 2008. The results (not
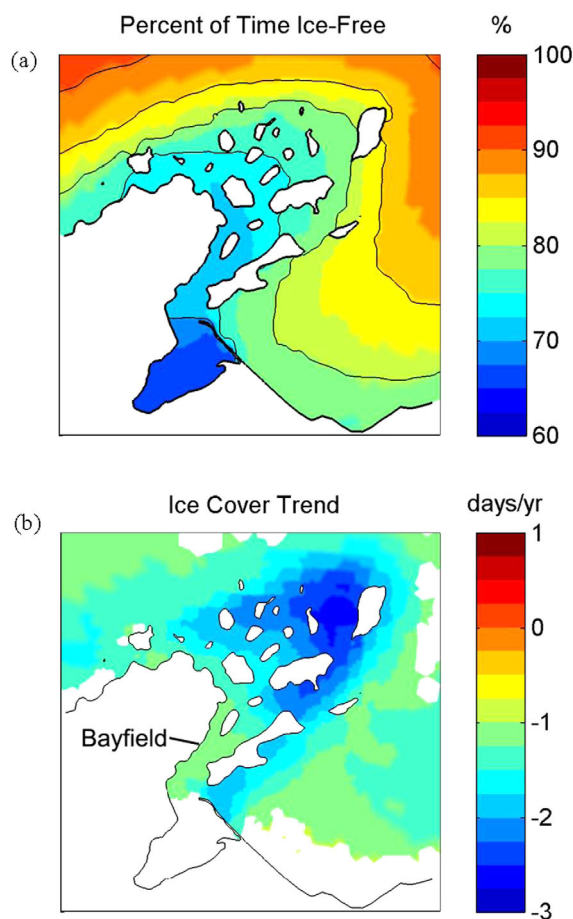
Figure 12. (a) Contour plot of the percent of time locations were ice free over the 35 year hindcast. Contours are drawn at 5% intervals. (b) Long-term trends in ice cover duration. Ice cover is defined as mean ice concentration greater than 30%. Only trends significant at 95% confidence are shaded.

shown for brevity) indicate that the percent differences in SWH statistics within the exterior are approximately equivalent to the percent of the wind scaling. Percent differences for SWHs statistics in the interior were approximately twice the wind scaling percentage, e.g., −20% difference in SWH for a wind scaling of −10%. Future study is suggested to improve the knowledge of winds within the interior of the Apostle Islands for the evaluation of wave climate.

5.2. Effects of Ice-Time on Wave Statistics

Ice-free wave climate statistics presented so far were estimated by omitting periods for ice concentrations greater than 30%. *Tuomi et al.* [2011] examined ice-free and ice-time included wave climate statistics. Each method of computing wave climate statistics has its own merits, depending on the application. We therefore adjust the reported ice-free statistics to include the ice-time, i.e., include the duration when SWH and PWP are zero. Figure 12a shows the percentage of time for the water was ice-free, yielding ice-time included mean SWHs that vary from 67% to 90% of those in Figure 6a. The range is caused by the spatial variation of ice cover in the Apostle Islands. Since quantile values cannot be adjusted in a similar manner, we adjust quantile percentage $Q_A = 100 - I_F(1 - Q/100)$, where Q is the original quantile percentage and I_F is the percentage of ice-free time. For a location that is ice free for 70% of the hindcast, the 0.90 and 0.99 quantiles adjust to the 0.93 and 0.993, respectively. Overall, ice-free and ice-time included statistics differ from each other based on the ice duration at a specific location. The largest differences occur in sheltered areas nearer to the mainland where ice duration is the longest.

5.3. Effects of Ice and Wind on Long-Term Wave Climate

Changes in ice cover can affect wave climate statistics by exposing waters to extreme winter storms [*Schwab et al.*, 2006]. NOAA ice charts used in this study are the most commonly used data set to examine decreasing ice cover trends in Lake Superior [*Austin and Colman*, 2007; *Wang et al.*, 2012]. Figure 12b shows the long-term trends in annual ice cover duration based on the threshold of 30% ice concentration applied in this study. All trends show that ice cover decreased over the hindcast period with a range of −1.1 to −2.4 days/yr with the most distinguished trend occurring in the northeast of the Apostle Islands. Similarly large slopes, greater than −2.0 days/yr, are observed in many other coastal areas of Lake Superior (not shown here for brevity) and are greater than the lakewide average of −1.21 days/yr. Few alternative sources of ice data are available to compare with NOAA ice charts in the Apostle Islands. *Howk* [2009] used ferry navigation records at Bayfield (see Figure 12b) to calculate a decreasing ice cover trend of −1.47 days/yr over the years of 1975–2007. This compares well with the slope of −1.16 days/yr from the NOAA ice charts near Bayfield, considering the definition of ice cover and time periods are slightly different. Further investigation is needed to validate the accuracy of the NOAA ice charts in the Apostle Islands. Comparing trends in ice cover duration (Figure 12b) and trends in SWH (Figure 10), an obvious negative correlation exists, suggesting that the loss of ice cover is the dominant mechanism for an increasing wave climate in the Apostle Islands. This explains the relatively higher percentage increase in SWHs observed in this study compared to other studies where ice was not a factor [*Caires and Sterl*, 2005; *Dodet et al.*, 2010].

Winds can affect long-term trends in the wave climate. Wind speed and direction are the dominant cause for a changing wave climate in regions without ice cover [*Sterl and Caires*, 2005; *Dodet et al.*, 2010]. Annual mean winds for long-term trends at station DISW3 (Figure 1) can be compared with those predicted by CFSR. The analysis was conducted with the available observational record at DISW3 from 1984 to 2013. It is found that CFSR wind speeds do not show any statistically significant trends for either the raw or adjusted equivalent neutrally stable winds. Similarly, observed wind speeds showed no significant trend at DISW3, consistent with the analysis of summer winds by *Austin and Colman* [2007]. Annual mean wind directions are also examined for long-term trends. Surprisingly, the CFSR winds show a significant clockwise shift in the annual mean wind direction at a rate of 0.95 degrees/yr ($p = 0.005$) that closely matches the observed rate of 1.26 degrees/yr ($p = 0.013$). A more northerly wind direction likely contributes to the increased wave heights, observed in the results, as winds would be traversing a larger fetch (Need more compelling evidence, further analyze the wind record to see if events from the NE are more frequent). Similar results are obtained for CFSR winds at the off-shore buoy St. 45006 over the same time period, with no trend in wind speed but a clockwise rotation of wind direction at 0.85 degrees/yr ($p = 0.013$). Observed values at St. 45006 did not show a statistically significant trend in wind direction, perhaps because the buoy is removed and redeployed at different times each year for the winter season. In short, increasing SWHs observed in the hindcast in this study are likely due, in part, to long-term trends of wind direction and not wind speed.

5.4. Effects of Water Level and Wave Climate Trends on $\overline{\text{CWIH}}$

To isolate the impact of the changing wave climate on $\overline{\text{CWIH}}$, trends are recomputed using a constant MWL taken as the average water level over the hindcast. Under this scenario, each site has a positive trend in $\overline{\text{CWIH}}$ due to an increasing wave climate over the hindcast. Sites B4–B6 have p values less than 0.05, generally matching the spatial patterns of significant trends observed for the SWHs (Figure 10). Specifically site B6 once again has the largest trend of $\overline{\text{CWIH}}$s 0.0075 m/yr with a p value close to 0. To isolate the impact of the water level on $\overline{\text{CWIH}}$, we also obtain the trend of the $\overline{\text{CWIH}}$s at B6 for the scenario with a constant wave climate and changing water levels. The negative trend -0.0084 m/yr under this scenario is also significant with a p value 0.00001. Combining these two scenarios, the effects of an increasing wave climate at site B6 essentially offsets the effects of decreasing water levels on the $\overline{\text{CWIH}}$s, yielding the trend in Figure 11f. This relationship is found to be generally consistent when varying the beach slope and toe elevation at B6 over the range of values reported in *Swenson et al.* [2006]. When the beach slope is shallower than 3°, the water level trend begin to dominate the increasing wave climate, yielding less $\overline{\text{CWIH}}$ or bluff recession rates.

6. Summary and Conclusions

The wave climate of the Apostle Islands in Lake Superior was obtained using a 35 year hindcast from 1979 to 2013 from a SWAN wave model. The performance and limitation of the SWAN wave model were carefully addressed through sensitivity tests of spatial resolution and the comparisons against a phase-resolving nonhydrostatic model for reflection and diffraction processes. Wave statistics (SWH, PWP, and MWD) were analyzed at the mean, 0.90 quantile, 0.99 quantile, and maximum to examine common and energetic events. Extreme value analysis was performed to estimate the 1, 10, and 100 year return values of SWH. In general, a consistent spatial pattern was observed for each statistic of the SWHs and PWPs due to the effect of island sheltering. For SWHs, the values in the island interior were approximately half the SWHs experienced immediately off-shore of the islands for each statistic. PWPs were similar in magnitude for the interior and exterior for the mean (3.5 s), but the differences were greater for more energetic events, e.g., maximum PWPs were approximately 5–6 and 10 s for the interior and exterior, respectively. An exception to a consistent spatial pattern was at the eastern exterior region of the islands where refraction concentrated wave energy. In particular, the GS had the largest SWHs in the hindcast at 5.5 m, as well as, the greatest 100 year return value estimate of SWH, 6.9 m. Examination of MWDs showed that, for average conditions, spreading of waves around the islands causes MWDs to be more westerly in the west and more easterly in the east. During the most energetic events, MWDs were from the northeast due to strong winds aligned with the greatest fetch length.

Two scientific questions related to wave climate are addressed. First, the wave climate change due to the relative role of changing wind fields or ice covers over the past 35 years was revealed. Long-term trends in SWH were examined from the model hindcast results. Increasing trends in SWH were found to be statistically significant for most of the interior of the Apostle Islands but not in surrounding offshore waters. Trend

magnitudes increased from the mainland toward the offshore direction with peak trends at the northeast. Peak trend magnitudes of SWH were 0.45 cm/yr for the mean, 0.95 cm/yr for the 0.90 quantile, and 1.45 cm/yr for the 0.99 quantile. Ice cover durations were found to have statistically significant long-term trends ranging from −1.1 to −2.4 days/yr. Peak trends in ice cover duration and SWH occurred at the same location, suggesting that loss of ice cover is the dominant reason for increasing SWHs. Wind speeds showed no statistically significant long-term trends. However, wind direction showed a statistically significant clockwise shift of 0.95 degrees/yr. Shifting wind directions likely contributed to increasing SWHs due to an increased fetch from that direction. Second, potential bluff erosion affected by the change of wave climate and the trend of lower water levels in the Apostle Islands, Lake Superior was examined. In general it was found that the elevated wave climate essentially offsets the effects of decreasing water levels on the $\overline{\text{CWIH}}$. Other factor like beach slope can affect the relative role of the low water level trend and increasing wave climate on bluff recession. Overall the new wave climatology provided here will serve to examine the impacts of wave climate on occurrence of freak waves [*Wu and Yao*, 2004; *Dysthe et al.*, 2008], nearshore-offshore sediment transport [*Schwab et al.*, 2006; *Lin and Wu*, 2014], and lake trout [*Coberly and Horrall*, 1980; *Schram et al.*, 1995] in the future.

References

Aarnes, O. J., Ø. Breivik, and M. Reistad (2012), Wave Extremes in the Northeast Atlantic, *J. Clim.*, 25, 1529–1543.

Alves, J., A. Chawla, H. Tolman, D. Schwab, G. Lang, and G. Mann (2014), The operational implementation of a Great Lakes wave forecasting system at NOAA/NCEP, *Weather Forecasting*, 29, 1473–1497, doi:10.1175/WAF-D-12-00049.1.

Angel, J. R. (1995), Large-scale storm damage on the U.S. shores of the Great Lakes, *J. of Great Lakes Research*, 21(3), 287–293.

Ardhuin, F., and A. Roland (2012), Coastal wave reflection, directional spread, and seismoacoustic noise sources, *J. Geophys. Res.*, 117, C00J20, doi:10.1029/2011JC007832.

Assel, R. A. (2003), An electronic atlas of Great Lakes ice cover, NOAA Great Lakes Ice Atlas, Great Lakes Environ. Res. Lab., Ann Arbor, Mich. [Available at http://www.glerl.noaa.gov/data/ice/atlas.]

Assel, R. A. (2005), Great Lakes weekly ice cover statistics, *NOAA Tech. Memo. GLERL-133*, NOAA Great Lakes Environ. Res. Lab., Ann Arbor, Mich.

Assel, R. A., F. Quinn, and C. Stellinger (2004), Hydroclimatic factors of the recent record drop in Laurentian Great Lakes water levels, *Bull. Am. Meteorol. Soc.*, 85(8), 1143–115.

Austin, J. A., and S. M. Colman (2007), Lake Superior summer water temperatures are increasing more rapidly than regional air temperatures: A positive ice-albedo feedback, *Geophys. Res. Lett.*, 34, L06604, doi:10.1029/2006GL029021.

Bennington, V., G. A. McKinley, N. Kimura, and C. H. Wu (2010), General circulation of Lake Superior: Mean, variability, and trends from 1979 to 2006, *J. Geophys. Res.*, 115, C12015, doi:10.1029/2010JC006261.

Bishop, C., and M. Donelan (1987), Measuring waves with pressure transducers, *Coastal Eng.*, 11(4), 309–328.

Booij, N., R. C. Ris, and L. H. Holthuijsen (1999), A third-generation wave model for coastal regions: 1. Model description and validation, *J. Geophys. Res.*, 104(C4), 7649–7666, doi:10.1029/98JC02622.

Brown, E. A., C. H. Wu, D. M. Mickelson, and T. B. Edil (2005), Factors controlling rates of bluff recession at two sites on Lake Michigan, *J. Great Lakes Res.*, 31(3), 306–321.

Caires, S., and A. Sterl (2005), A new nonparametric method to correct model data: Application to significant wave height from the ERA-40 re-analysis, *J. Atmos. Oceanic Technol.*, 22(4), 443–459, doi:10.1175/JTECH1707.1.

Castedo, R., M. Fernandez, A. S. Trendhaile, and C. Paredes (2013), Modeling cyclic recession of cohesive clay coasts: Effects of wave erosion and bluff stability, *Mar. Geol.*, 335, 162–176.

Chawla, A., D. M. Spindler, and H. L. Tolman (2013), Validation of a thirty year wave hindcast using the Climate Forecast System Reanalysis winds, *Ocean Modell.*, 70, 189–206, doi:10.1016/j.ocemod.2012.07.005.

Choulakian, V., and M. Stephens (2001), Goodness-of-fit test for the generalized Pareto distribution, *Technometrics*, 43, 478–485, doi: 10.1198/00401700152672573.

Coberly, C. E., and R. M. Horrall (1980), Fish spawning grounds in Wisconsin waters of the Great Lakes, *Rep. WIS-SG-80–235*, Univ. of Wis. Sea Grant Inst., Madison, Wis.

Coles, S. (2001), *An Introduction to Statistical Modeling of Extreme Values*, Springer, London, U. K.

Desai, A. R., J. A. Austin, V. Bennington, and G. A. McKinley (2009), Stronger winds over a large lake in response to weakening air-to-lake temperature gradient, *Nat. Geosci.*, 2, 855–858, doi:10.1038/ngeo693.

Dodet, G., X. Bertin, and R. Taborda (2010), Wave climate variability in the North-East Atlantic Ocean over the last six decades, *Ocean Modell.*, 31, 120–131, doi:10.1016/j.ocemod.2009.10.010.

Dysthe, K., H. E. Krogstad, and P. Muller (2008), Oceanic rogue waves, *Annu. Rev. Fluid Mech.*, 40, 287–310.

Elgar, S., T. H. C. Herbers, and R. T. Guza (1994), Reflection of ocean surface gravity waves from a natural beach, *J. Phys. Oceanogr.*, 24(7), 1503–1511, doi:10.1175/1520-0485(1994)024<1503:ROOSGW>2.0.CO;2.

Fitzsimons, J. D., and J. E. Marsden (2014), Relationship between lake trout spawning, embryonic survival, and currents: A case of bet hedging in the face of environmental stochasticity, *J. Great Lakes Res.*, 40, 92–101, doi:10.1016/j.jglr.2013.12.014.

Gorman, R. M., K. R. Bryan, and A. K. Laing (2003), Wave hindcast for the New Zealand region: Nearshore validation and coastal wave climate, *N. Z. J. Mar. Freshwater Res.*, 37, 567–588.

Gronewold, A. D., V. Fortin, B. Lofgren, A. Clites, C. A. Stow, and F. Quin (2013), Coasts, water levels, and climate change: A Great Lakes perspective, *Clim. Change*, 120, 697–711.

Hasselmann, K., D. B. Ross, P. Muller, and W. Sell (1976), A parametric wave prediction model, *J. Phys. Oceanogr.*, 6(2), 200–228.

Holthuijsen, L. H., A. Herman, and N. Booij (2003), Phase-decoupled refraction–diffraction for spectral wave models, *Coastal Eng.*, 49, 291–305, doi:10.1016/S0378–3839(03)00065-6.

Howk, F. (2009), Changes in Lake Superior ice cover at Bayfield, Wisconsin, *J. Great Lakes Res.*, 35, 159–162, doi:10.1016/j.jglr.2008.11.002.

Hubertz, J. M., D. B. Driver, and R. D. Reinhard (1991), Wind waves on the Great Lakes: A 32 year hindcast, *J. Coastal Res.*, 7, 945–967.

Jensen, R. E., M. A. Cialone, R. S. Chapman, B. A. Ebersole, M. Anderson, and L. Thomas (2012), Lake Michigan storm: Wave and water level modeling, *Tech. Rep. ERDC/CHL TR-12-26*, Coastal and Hydraul. Lab., U.S. Army Eng. Res. and Dev. Cent., Vicksburg, Miss.

Jones, N. L., and S. G. Monismith (2007), Measuring short-period wind waves in a tidally forced environment with a subsurface pressure gauge, *Limnol. Oceanogr. Methods*, *5*, 317–327.

Kraft, G. J., C. Mechenich, D. J. Mechenich, and S. W. Szczytko (2007), Assessment of coastal water resources and watershed conditions at Apostle Islands National Lakeshore, Wisconsin, *Nat. Resour. Tech. Rep. NPS/NRWRD/NRTR—2007/367*, Natl. Park Serv., Fort Collins, Colo. [Available at http://www.nature.nps.gov/water/nrca/assets/docs/apis_coastal.pdf.]

Lin, J. G. (2013), An improvement of wave refraction-diffraction effect in SWAN, *J. Mar. Sci. Technol.*, *21*(2), 198–208, doi:10.6119/JMST-012-1207-1.

Lin, Y. T., and C. H. Wu (2014), A field study of nearshore environmental changes in response to newly-built coastal structures in Lake Michigan, *J. Great Lakes Res.*, *40*, 102–114, doi:10.1016/j.jg1r.2013.12.013.

Liu, P.C., and D. B. Ross (1980), Airborne measurements of wave growth for stable and unstable atmospheres in Lake Michigan, *J. Phys. Oceanogr.*, *10*, 1842–1853, doi:10.1175/1520-0485(1980)010<1842:AMOWGF>2.0.CO;2.

Liu, P. C., and D. J. Schwab (1987), A comparison of methods for estimating u^* from given u_z and air-sea temperature differences, *J. Geophys. Res.*, *92*(C6), 6488–6494, doi:10.1029/JC092iC06p06488.

Liu, P. C., D. J. Schwab, and J. R. Bennett (1984), Comparison of a two-dimensional wave prediction model with synoptic measurements in Lake Michigan, *J. Phys. Oceanogr.*, *14*(9), 1514–1518, doi:10.1175/1520-0485(1984)014<1514:COATDW>2.0.CO;2.

McLeod, A. I., K. W. Hipel, and B. A. Bodo (1990), Trend analysis methodology for water quality time series, *Environmetrics*, *2*, 169–200.

Meadows, G. A., L. A. Meadows, W. L. Wood, J. M. Hubertz, and M. Perlin (1997), The relationship between great lakes water levels, wave energies, and shoreline damage, *Bull. Am. Meteorol. Soc.*, *78*, 675–683, doi:10.1175/1520-0477(1997)078<0675:TRBGLW>2.0.CO;2.

Melby, J. (2012), Wave runup prediction for flood hazard assessment, *Rep*. ERDC/CHL TR-12–24, Coastal and Hydraul. Lab., U.S. Army Eng. Res. and Dev. Cent., Vicksburg, Miss.

Nortek AS (2005), *AWAC: Acoustic Wave and Current Meter, User Guide, N3000-126*, Revision E, Norway.

O'Reilly, W. C., R. T. Guza, and R. J. Seymour (1999), Wave prediction in the Santa Barbara channel, final technical report, pp. 76–80, Pac. Outer Cont. Shelf Reg., Miner. Manage. Serv., U.S. Dep. of the Interior, Washington, D. C.

Panchang, V., C. K. Jeong, and Z. Demirbilek (2013), Analyses of extreme wave heights in the Gulf of Mexico for offshore engineering applications, *J. Offshore Mech. Arctic Eng.*, *135*(3), 031104, doi:10.1115/1.4023205.

Panchang, V. G., C. Jeong, and D. Li (2008), Wave climatology in coastal Maine for aquaculture and other applications, *Estuaries Coasts*, *31*(2), 289–299, doi:10.1007/s12237-007-9016-5.

Pendleton, E. A., E. R. Thieler, and S. J. Williams (2007), Coastal change-potential assessment of Sleeping Bear Dunes, Indiana Dunes, and Apostle Islands National Lakeshores to lake-level changes, 48 pp., *U.S. Geol. Surv. Open File Rep., 2005-1249*. [Available at http://pubs.usgs.gov/of/2005/1249/images/pdf/report.pdf.]

Ponce de Leon, S., and C. Guedes Soares (2010), The sheltering effect of the Balearic Islands in the hindcast wave field, *Ocean Eng.*, *37*, 603–610, doi:10.1016/j.oceaneng.2010.01.011.

Resio, D. T., and C. L. Vincent (1978), Design wave information for the Great Lakes, Report 5, Lake Superior, *WES Tech. Rep. H-76-1*, U.S. Army Eng. Waterw. Exp. Stn., Vicksburg, Miss.

Ris, R. C., N. Booij, and L. H. Holthuijsen (1999), A third-generation wave model for coastal regions: 2. Verification, *J. Geophys. Res.*, *104*(C4), 7667–7681.

Rusu, E., and C. Guedes Soares (2012), Wave energy pattern around the Madeira Islands, *Energy*, *45*, 771–785, doi:10.1016/j.energy.2012.07.013.

Rusu, E., P. Pilar, and C. Guedes Soares (2008), Evaluation of the wave conditions in Madeira archipelago with spectral models, *Ocean Eng.*, *35*(13), 1357–1371, doi:10.1016/j.oceaneng.2008.05.007.

Saha, S., et al. (2010), The NCEP climate forecast system reanalysis, *Bull. Am. Meteorol. Soc.*, *91*, 1015–1057, doi:10.1175/2010BAMS3001.1.

Saha, S., et al. (2014), The NCEP climate forecast system version 2, *J. Clim.*, *27*, 2185–2208, doi:10.1175/JCLI-D-12-00823.1.

Schram, S. T., J. H. Selgeby, C. R. Bronte, and B. L. Swanson (1995), Population recovery and natural recruitment of lake trout at Gull Island Shoal, Lake Superior, 1964–1992, *J. Great Lakes Res.*, *21*, 225–232.

Schwab, D. J., B. J. Eadie, R. A. Assel, and P. J. Roebber (2006), Climatology of large sediment resuspension events in southern Lake Michigan, *J. Great Lakes Res.*, *32*, 50–62, doi:10.3394/0380–1330(2006)32[50:COLSRE]2.0.CO;2.

Siadatmousavi, S. M., F. Jose, and G. W. Stone (2011), The effects of bed friction on wave simulation: Implementation of an unstructured third-generation wave model, SWAN, *J. Coastal Res.*, *27*(1), 140–152.

Sorensen, R. M. (2006), *Basic Coastal Engineering*, 3rd ed., Springer, N. Y.

Sterl, A., and S. Caires (2005), Climatology, variability and extrema of ocean waves: The web-based KNMI/ERA-40 wave atlas, *Int. J. Climatol.*, *25*(22), 963–977, doi:10.1002/joc.1175.

Stopa, J. E., K. F. Cheung, H. L. Tolman, and A. Chawla (2013a), Patterns and cycles in the Climate Forecast System Reanalysis wind and wave data, *Ocean Modell.*, *70*, 207–220, doi:10.1016/j.ocemod.2012.10.005.

Stopa, J. E., J. F. Filipot, N. Li, K. F. Cheung, and Y. L. Chen (2013b), Wave energy resources along the Hawaiian Island chain, *Renewable Energy*, *55*, 305–321, doi:10.1016/j.renene.2012.12.030.

SWAN Team (2013), *Swan Cycle III Version 40.91A, Scientific and Technical Documentation*, Delft Univ. of Technol., Delft, Netherlands.

Swenson, M. J., C. H. Wu, T. B. Edil, and D. M. Mickelson (2006), Bluff recession rates and wave impact along the Wisconsin coast of Lake Superior, *J. Great Lakes Res.*, *32*, 512–530, doi:10.3394/0380-1330(2006)32[512:BRRAWI]2.0.CO;2.

Thomasen, S., J. Gilbert, and P. Chow-Fraser (2013), Wave exposure and hydrologic connectivity create diversity in habitat and zooplankton assemblages at nearshore Long Point Bay, Lake Erie, *J. Great Lakes Res.*, *39*, 56–65, doi:10.1016/j.jglr.2012.12.014.

Tuomi, L., K. K. Kahma, and H. Pettersson (2011), Wave hindcast statistics in the seasonally ice-covered Baltic Sea, *Boreal Environ. Res.*, *16*, 451–472.

Tuomi, L., H. Pettersson, C. Fortelius, T. Kimmo, J. V. Bjorkqvist, and K. K. Kahma (2014), Wave modelling in archipelagos, *Coastal Eng.*, *85*, 205–220, doi:10.1016/j.coastaleng.2013.10.011.

Wang, J., X. Bai, H. Hu, A. Clites, M. Colton, and B. Lofgren (2012), Temporal and spatial variability of Great Lakes ice cover, 1973–2010, *J. Clim.*, *25*, 1318–1329, doi:10.1175/2011JCLI4066.1.

Wang, X. L., and V. R. Swail (2002), Trends of Atlantic wave extremes as simulated in a 40-year wave hindcast using kinematically reanalyzed wind fields, *J. Clim.*, *15*(9), 1020–1035.

Waters, R., J. Engstrom, J. Isberg, and M. Leijon (2009), Wave climate off Swedish west coast, *Renewable Energy*, *34*(6), 1600–1606, doi:10.1016/j.renene.2008.11.016.

World Meteorological Organization (2007), The role of climatological normals in a changing climate, *Rep. WCDMP-61*, Geneva, Switzerland.

Wu, C. H., and A. F. Yao (2004), Laboratory measurements of limiting freak waves on currents, *J. Geophys. Res.*, *109*, C12002, doi:10.1029/2004JC002612.

Wu, C. H., C. C. Young, Q. Chen, and P. J. Lynett (2010), Efficient nonhydrostatic modeling of surface waves from deep to shallow water, *J. Waterw. Port Coastal Ocean Eng.*, *136*(2), 104–118, doi:10.1061/_ASCE_WW.1943-5460.0000032.

Young, C. C., C. H. Wu, W. C. Liu, and J. T. Kuo (2009), A higher-order non-hydrostatic sigma model for simulating non-linear refraction-diffraction of water waves, *Coastal Eng.*, *56*(9), 919–930.

Yuan, H. L., and C. H. Wu (2006), Fully non-hydrostatic modeling of surface waves, *J. Eng. Mech.*, *132*(4), 447–456.

Zijlema, M. (2010), Computation of wind-wave spectra in coastal waters with SWAN on unstructured grids, *Coastal Eng.*, *57*, 267–277, doi:10.1016/j.coastaleng.2009.10.011.